New determination of the gravitational constant G with time-of-swing method

Article *in* Physical review D: Particles and fields · July 2010

DOI: 10.1103/PHYSREVD.82.022001

8 authors, including:

Liang-Cheng Tu
Huazhong University of Science and Technology
71 PUBLICATIONS **715** CITATIONS
SEE PROFILE

Chenggang Shao
Huazhong University of Science and Technology
26 PUBLICATIONS **150** CITATIONS
SEE PROFILE

Qi Liu
Sun Yat-Sen University
21 PUBLICATIONS **281** CITATIONS
SEE PROFILE

New determination of the gravitational constant G with time-of-swing method

Liang-Cheng Tu, Qing Li, Qing-Lan Wang, Cheng-Gang Shao, Shan-Qing Yang, Lin-Xia Liu, Qi Liu, and Jun Luo*

Department of Physics, Huazhong University of Science and Technology, Wuhan 430074, People's Republic of China

(Received 25 March 2010; published 1 July 2010)

A new determination of the Newtonian gravitational constant G is presented by using a torsion pendulum with the time-of-swing method. Compared with our previous measurement with the same method, several improvements greatly reduced the uncertainties as follows: (i) two stainless steel spheres with more homogeneous density are used as the source masses instead of the cylinders used in the previous experiment, and the offset of the mass center from the geometric center is measured and found to be much smaller than that of the cylinders; (ii) a rectangular glass block is used as the main body of the pendulum, which has fewer vibration modes and hence improves the stability of the period and reduces the uncertainty of the moment of inertia; (iii) both the pendulum and source masses are placed in the same vacuum chamber to reduce the error of measuring the relative positions; (iv) changing the configurations between the ''near'' and ''far'' positions is remotely operated by using a stepper motor to lower the environmental disturbances; and (v) the anelastic effect of the torsion fiber is first measured directly by using two disk pendulums with the help of a high-Q quartz fiber. We have performed two independent G measurements, and the two G values differ by only 9 ppm. The combined value of G is $(6.673\,49 \pm 0.000\,18) \times 10^{-11}$ m^3 kg^{-1} s^{-2} with a relative uncertainty of 26 ppm.

DOI: 10.1103/PhysRevD.82.022001 PACS numbers: 06.20.Jr, 04.80.Cc

I. INTRODUCTION

A. Background

Based on careful observations of senior scientists, Isaac Newton realized that the motion of the planets obeyed the same intrinsic law as that of the falling apple, which was published in the epochal literature ''*Philosophiae Naturalis Principia Mathematica*'' in 1687 [1], and presented the celebrated law of universal gravitation as

$$F = G\frac{Mm}{r^2}, \tag{1}$$

where F is the gravitational force acting between masses M and m, the centers of mass of which are separated by the distance r. The constant of proportionality G is named as the *universal gravitational constant* because it is thought to be the same at all places and all times and thus universally characterizes the intrinsic strength of the gravitational force. The value of G tells us: how strong the gravitational force is between two masses separated by r, how much the space-time is curved in Einstein's theory of general relativity, where G is a scale factor appearing in the field equations, and what the mass and the mean density of the Earth, Moon, Sun, and other planets will be, where one needs the value of G to obtain the mass of the planet M from the product GM.

The experimental and theoretical research on gravitational interaction has always been an active field because of its importance to our understanding of the nature at the most fundamental level [2–4]. Dirac's ''large numbers hypothesis'' [5,6], which questions the very constancy of fundamental physical constants, further inspires deeper experimental and theoretical studies on gravitation and the large scale structure of our Universe. Improved knowledge of G could play an important role in successfully unifying the four fundamental forces [7–9]. Besides, many theoretical models anticipate that the space-time variability of the fundamental constants, specifically the gravitational constant G, could be related to the expansion of the Universe, depending on the cosmological model considered [10,11], and the spatial or temporal gradients in the value of G have been searched by using the lunar and planetary ranging measurements with an accuracy at the level of $\dot{G}/G = (5 \pm 6) \times 10^{-13}$ yr^{-1} [12,13]. However, the present situation of our knowledge on the absolute value of G is an embarrassment to modern physics. As one of the most important fundamental constants in nature, the accuracy of the absolute value of G is still the worst one. The present uncertainty in G is thousands of times larger than that of other important fundamental constants, such as the Planck constant h, the fine-structure constant α, the elementary charge e, etc.

The absolute value of G was first measured in the laboratory by Cavendish in 1798 [14], more than 100 years after Newton presented his law of universal gravitation. Cavendish reported his results in a paper entitled ''*Experiments to determine the density of the Earth*'' and gave $G = 6.67(7) \times 10^{-11}$ m^3 kg^{-1} s^{-2} with a relative uncertainty (u_r) of about 1%. Over the past two centuries, nearly 300 different values of G have appeared; however, the measurement precision of the G value has improved only at the rate of about 1 order of magnitude per century.

In 2006, the Committee on Data for Science and Technology (CODATA), based on the weighted mean of

*junluo@mail.hust.edu.cn

eight values obtained in the previous few years, recommended an updated G value of $G_{2006} = 6.674\,28(67) \times 10^{-11}\ \mathrm{m^3\,kg^{-1}\,s^{-2}}$ with a relative standard uncertainty $u_r = 100$ ppm (parts per million) [15], which is two-thirds that of the 2002 CODATA adjustment [16]. The situation of the G measurement has been improved considerably since the 1998 CODATA adjustment [17]. However, the adopted values in CODATA-2006 are still in poor agreement with the claimed uncertainties of the eight G experiments. For example, Karagioz and Izmailov [18] at Tribotech Research and Development Company in Russia (TR&D-96, the abbreviation cited in the 2006 CODATA adjustment [15], hereinafter the same) obtained a value for G with $u_r = 75$ ppm, which is 208 ppm lower than the 2006 recommended value G_{2006}; Hu, Guo, and Luo [19] at Huazhong University of Science and Technology in China (HUST-05) found a value with $u_r = 130$ ppm, which is 297 ppm lower; Armstrong and Fitzgerald [20] at Measurement Standards Laboratory in New Zealand (MSL-03) gave a value with $u_r = 40$ ppm, which is 61 ppm lower; and Quinn *et al.* [21] at International Bureau of Weights and Measures in France (BIPM-01) measured a value with $u_r = 40$ ppm, which is 196 ppm larger. Only the other four G values: LANL-97 with $u_r = 105$ ppm [22], Uwash-00 with $u_r = 14$ ppm (the most precise value up to the present) [23], UWup-02 with $u_r = 147$ ppm [24], and UZur-06 with $u_r = 18$ ppm [25,26] fall within the uncertainty of G_{2006}.

The disagreement between the measured G values implies that the uncertainty could be larger than that assigned by the 2006 adjustment. The fact that this famous fundamental constant is still so poorly known testifies to the difficulty of the G measurement due to the extreme weakness and nonshieldability of gravity, and difficulties in determining the dimensions and density distributions of the bodies involved with sufficient accuracy, and hence challenges experimental physicists to make a more reliable determination of G by reducing systematic errors further.

Here we report our new determination of G by means of the time-of-swing method, some of which has already appeared in a Letter [27], and this paper presents a complete description of the apparatus, experimental techniques, and analysis methods. Using the same method, a preliminary result was reported in 1998 [28], which was named as HUST-99 in the 1998 and 2002 CODATA adjustments. In our following work, two systematic errors, the offset of the center-of-mass (CM) from the geometric center (GC) of the two cylindrical source masses and the effect of the air buoyancy, were found and corrected [19]. This is named as HUST-05 in the 2006 CODATA adjustment. The corrected G value was still model-dependent on the density distribution of the cylinders. Based on several further improvements, the uncertainty is greatly reduced in the latest measurement compared with our previous G values.

B. Time-of-swing method

The time-of-swing method, developed by Heyl [29] in the 1920s, has been commonly used to measure G [18,22,28,30–34]. In this method, a torsion pendulum is suspended by a very thin fiber, and two source masses are placed on opposite sides of the pendulum, as shown in Fig. 1. In their absence, the pendulum's free oscillation frequency squared ω_0^2 is related to the pendulum's moment of inertia I and the fiber's torsion constant K by

$$\omega_0^2 = \frac{K}{I}. \tag{2}$$

Because of the gravitational interaction between the pendulum and the source masses, the oscillation frequency of the torsion pendulum would change slightly. The torque on the pendulum when rotated by an angle θ from its equilibrium position is the sum of a torque $-K\theta$ produced by the twisted fiber and a torque $\tau_g(\theta)$ from gravitational interaction with the source masses. The torque $\tau_g(\theta)$ may be expanded as

$$\tau_g(\theta) = -K_{1g}\theta - K_{3g}\theta^3 + O(\theta^5), \tag{3}$$

where $K_{1g} = \frac{\partial^2 V_g(\theta)}{\partial\theta^2}$ and $K_{3g} = \frac{1}{6}\frac{\partial^4 V_g(\theta)}{\partial\theta^4}$ evaluated at the "near" position ($\theta = 0$) or the "far" position ($\theta = \pi/2$), with $V_g(\theta)$ being the gravitational potential energy between the pendulum and the source masses. For a small oscillation, K_{3g} and higher terms are neglectable, and we may treat K_{1g} as the effective gravitational torsion constant. Then we may write it as GC_g, where C_g is determined by the mass distributions of the pendulum and source masses. Therefore, the frequency squared of the pendulum in the presence of the source masses at the near or far position is

$$\omega_n^2 = \frac{K_n + GC_{gn}}{I}, \tag{4}$$

$$\omega_f^2 = \frac{K_f + GC_{gf}}{I}, \tag{5}$$

respectively, where the subscript n and f denote the near

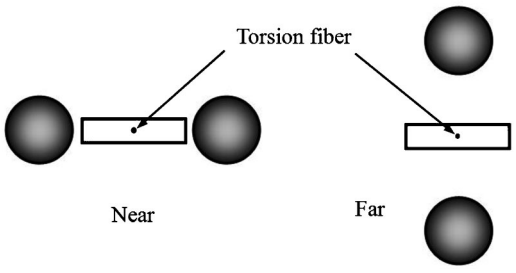

FIG. 1. Top view of the two configurations of the pendulum and source masses in the time-of-swing method. At the near position, the equilibrium position of the pendulum is in line with the source masses, and at the far position, it is perpendicular.

and far positions, respectively. For an ideal torsion fiber, namely, $K_n \equiv K_f$, one requires no knowledge of the torsion fiber's constant and then G could be determined by

$$G = \frac{I(\omega_n^2 - \omega_f^2)}{C_{gn} - C_{gf}} = \frac{I\Delta(\omega^2)}{\Delta C_g}. \quad (6)$$

The most distinct feature of the time-of-swing method is that it converts the weak gravitational interaction into a frequency change, which could be measured with a resolution much better than that of force, and the result is independent of the value of the fiber's torsion constant. However, for a nonideal torsion fiber, the major shortcoming is the need to know the fiber's properties with sufficient accuracy, such as its response to the ambient temperature, the pendulum's oscillation amplitude and frequency, time, etc. Another difficulty, just like in measuring G with other methods, is determining the dimensions and the density distribution of the masses with sufficient accuracy.

C. Parameterizations

A schematic drawing of the pendulum system is shown in Fig. 2. The main body of the pendulum is suspended by a 25-μm-diameter, 890-mm-long tungsten fiber, which hangs from a passive magnetic damper consisting of a copper disk and an aluminum shaft. The magnetic damper is suspended in a cylindrically symmetric magnetic field produced by a ring magnet. The upper end of the damper shaft then hangs from a 50-μm-diameter, 90-mm-long prehanger tungsten fiber. This magnetic damper is used to reduce the tilt-twist coupling to the pendulum [35–37].

Because of the existence of the magnetic damper, the mathematical model for G measurement becomes (a detailed derivation is given in Appendix A)

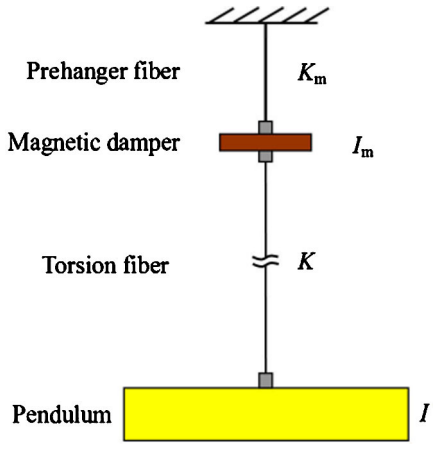

FIG. 2 (color online). Schematic diagram of the two-stage pendulum used in our G measurement. The magnetic damper and the pendulum, suspended by the prehanger fiber and torsion fiber, respectively, consist of a passive vibration isolation system for the swing and wobble modes of the pendulum, while the damper's axial symmetry minimizes the damping of the torsional motion of the pendulum.

$$G = \frac{I\Delta(\omega^2)}{\Delta C_g}\left[1 - \frac{\Delta K}{I\Delta(\omega^2)} + \frac{I_m}{I}\frac{K^2(\omega_n)}{K_m^2}\right], \quad (7)$$

where $\Delta K = K_n - K_f$ denotes the correction of the fiber's anelasticity. The spring constant of the torsion fiber K is a function of oscillation frequency, as proposed by Kuroda [38]. I_m and K_m represent the moment of inertia of the magnetic damper and the torsion constant of the prehanger fiber, respectively, and the last term in the square brackets is the correction from the magnetic damper.

D. Outline

In our present G measurement, several improvements have been made to reduce the uncertainties compared to our previous experiment [28]: (i) the spherical source masses with more homogeneous density are used to replace the cylinders, and the offset of the CM from the GC is greatly reduced; (ii) the pendulum body is a rectangular glass, which has fewer vibration modes and hence improves the stability of the period and reduces the uncertainty of the moment of inertia; (iii) both the pendulum and source masses are placed in the same vacuum chamber to reduce the error of measuring the relative positions; (iv) changing the configurations between the near and far positions is remotely operated by using a stepper motor to lower the environmental disturbances; and (v) the anelastic effect of the torsion fiber is first measured directly by using two disk pendulums with the help of a high-Q quartz fiber.

The organization of this paper is as follows: the experimental apparatus and procedures used to determine the dimensions and the density inhomogeneity of the masses and to position and align the masses are covered in Sec. II. These measurements will be used to determine parameters I and ΔC_g in Eq. (7), in which the distance between the centers of the two source masses and the inhomogeneity of the coating layer on the pendulum body contribute the dominant uncertainty. In Sec. III, the data acquisition system is described. The systematic effects, including the properties of the fiber, gravitational nonlinearity of the source mass, and external electrostatic and magnetic effects, are studied in detail in Sec. IV. Measuring the anelastic property of the torsion fiber, $\Delta K/I\Delta(\omega^2)$ in Eq. (7), brings the biggest uncertainty and correction in the present experiment. Section V describes the analysis method of the pendulum's angle-time data, which yields the parameter $\Delta(\omega^2)$ in Eq. (7). The experimental results of our G measurements are given in Sec. VI, and a brief discussion is presented in Sec. VII.

In the present G experiment, two independent measurements are made by two separate subgroups successively from 2005 to 2008. We designate them as experiments I and II. The pendulum system and source masses (the spheres) are common in the two experiments. In experiment II, the positions of the source masses are exchanged

and their orientations are changed deliberately. The surface separation of the spheres is remeasured, and the relative positions between the source masses and the pendulum are also adjusted and redetermined in experiment II.

II. APPARATUS

A. General description

Figures 3 and 4 show a cutaway view of our G measurement and photographs of our experimental apparatus, respectively. The heart of the apparatus is a two-stage pendulum system, which is suspended from the top of the electrically grounded vacuum chamber by a rotational feedthrough. The pendulum twist is monitored by an optical lever outside the vacuum chamber.

The source masses are two SS316 stainless steel spheres. Four small identical Zerodur rings, two of them supporting the source masses and the others acting as the gravitational counterbalances, are symmetrically adhered on a Zerodur disk of 240-mm diameter and 25-mm thickness. The Zerodur disk is mounted on a turntable driven by a stepper motor [39]. Because of the extremely low thermal expansion coefficient of Zerodur, $(0 \pm 1) \times 10^{-7}/°\mathrm{C}$, the variation of the separation between the mass centers of the source masses caused by the temperature fluctuations is negligible. The Zerodur rings and the disk are coated with a thin layer of aluminum to keep the source masses well grounded in experiment I. Because of frequent handling of the Zerodur disk in subsequent measurements, most of the aluminum layer has been scraped off by the time experiment I is finished. Therefore, a thin layer of aluminum foil is used to cover the Zerodur rings and the disk for grounding in experiment II (as shown in Fig. 4). This causes a slightly larger separation between the two spheres than in experiment I. A thin hollow gold-coated aluminum cylinder is inserted between the pendulum and the source masses for electrostatic shielding, which seems to improve the stability of the pendulum's period.

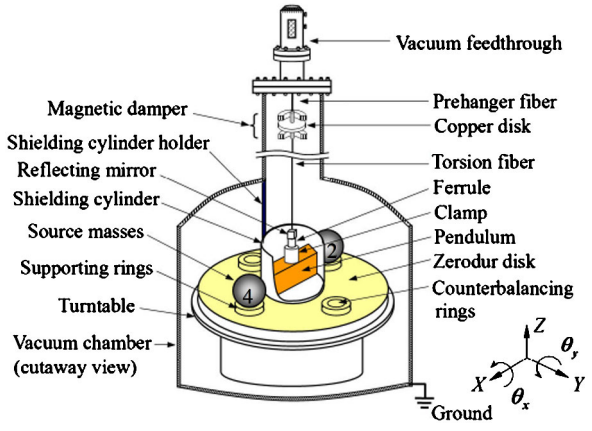

FIG. 3 (color online). A cutaway view of the two-stage pendulum system and source masses in our G measurement. The coordinate axes in the laboratory frame are also shown.

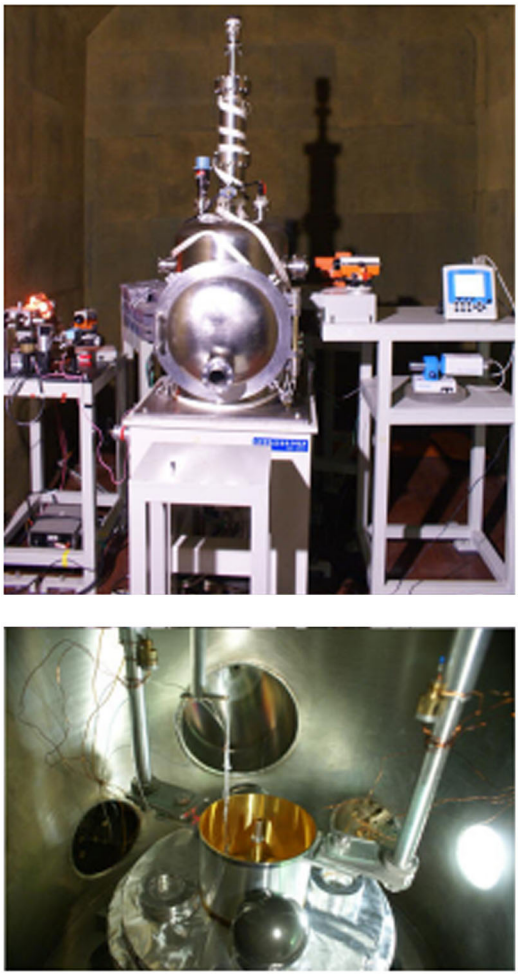

FIG. 4 (color online). The upper photo shows an external view of the entire experimental apparatus. The lower photo shows the suspended pendulum and source masses in the vacuum chamber in experiment II. A thin hollow gold-coated aluminum cylinder is inserted between them for electrostatic shielding.

The main body of the vacuum chamber is a stainless steel cylinder with an inner diameter of 450 mm and a height of 500 mm. A rotary vane pump [40] and a turbomolecular pump [41] at the bottom of the chamber are used to acquire vacuum, and an ion pump [42], located behind the vacuum chamber, is used to maintain a pressure of $\sim 10^{-5}$ Pa in the chamber during the experiments. Three optical telescopes, mounted on separate tables free from the vacuum chamber, are used to monitor the changes in the pendulum's position from air to the vacuum condition. Two of them, aimed at the fiber in two mutually perpendicular directions, and the third one, aimed at the pendulum, monitored the change in the vertical direction. Six temperature sensors with four inside the chamber, two tiltmeters in two orthogonal directions, and one barometer are used to monitor the temperature variations of the

environment, tilt of the chamber, and fluctuations of the air pressure, respectively.

The apparatus is located in a mu-metal shielded room of $5 \times 3 \times 3.5$ m^3 in dimension, which is installed on a shock-proof platform weighing about 24 tons. About 3 m below our laboratory, there is an electrical ground net connected with thick copper plates and wires. The laboratory is located inside Yujia Mountain, north of our campus (HUST). The laboratory is over 40 m underground, and the nearest exit is at the foot of the mountain and 150 m away from the laboratory. The temperature remains around 20°C all year round without any control. The daily change of temperature in the shielded room of our laboratory is less than 0.005°C, and the annual fluctuation is about 1 °C [43].

B. Laboratory coordinate system

Here we define the laboratory coordinate system (X, Y, Z), shown in Fig. 3. The origin O is at the CM of the pendulum system, which consists of the pendulum body, clamp, ferrule, and mirror. The vertical Z axis points along the main (25-μm-diameter) torsion fiber. The horizontal X axis points from the no. 2 sphere to no. 4, as shown in Fig. 3. The horizontal Y axis is defined by the right-handed coordinate system. The θ_X and θ_Y, describing the attitude of the pendulum, are defined as angles about the X and Y axes in the counterclockwise direction.

The laboratory coordinate system defined above assumes that the torsion fiber is completely flexible and massless. This means that the extended line of the fiber passes through the CM of the pendulum system O, even if the suspended pendulum is tilted, as shown in the left-hand drawing of Fig. 5. In Sec. II E 5, we check this assumption and find it reasonable by measuring the deviation of the GC of the clamp O_1 with respect to the torsion fiber.

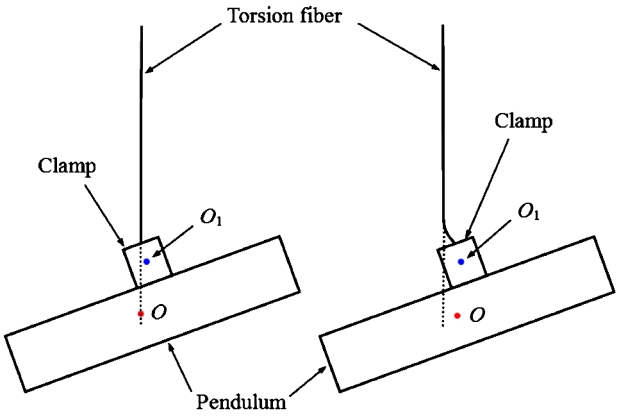

FIG. 5 (color online). The left-hand figure displays that the torsion fiber is completely flexible, in which its extended line passes through the CM of the pendulum system O, even if the pendulum is hung tilted. The right-hand figure shows the case for an incompletely flexible torsion fiber. O_1 is the GC of the clamp.

To calculate the parameters I and ΔC_g in Eq. (7) more conveniently, another coordinate system fixed to the pendulum body is used, and the transformation between the two frames is shown in Appendix B.

C. The two-stage pendulum system

The two-stage pendulum system consists of the magnetic damper and pendulum that are hung from the prehanger fiber and torsion fiber, respectively, as shown in Fig. 6. The pendulum contains the rectangular glass block with a thin layer of gold coating, the aluminum clamp and ferrule, and the mirror. The cylindrical clamp, glued to the center of the top surface of the pendulum body, is connected to the cylindrical ferrule. The mirror, which is a gold-coated cubical glass, is glued to the center of the ferrule and is used to reflect the laser beam monitoring the pendulum twist. The bottom end of the torsion fiber, passing through the thin holes on the mirror and ferrule, is knotted and nested at the end of the circular cone in the ferrule by epoxy. Because of the symmetric configuration of the clamp, ferrule, and mirror, their gravitational torques are extremely small. In the following subsections, we will discuss in detail the properties of each component in the two-stage pendulum system.

1. Torsion fibers

There are two pieces of tungsten fiber in our pendulum system. The prehanger fiber is a 90-mm-long, 50-μm-diameter annealed tungsten fiber [44], which is attached to a vacuum feedthrough at the top of the vacuum chamber for suspending the magnetic damper. The main torsion fiber is an 890-mm-long, 25-μm-diameter annealed tungsten wire (tungsten 99.4/thorium 0.6) [44], which hangs from the magnetic damper. The main fiber

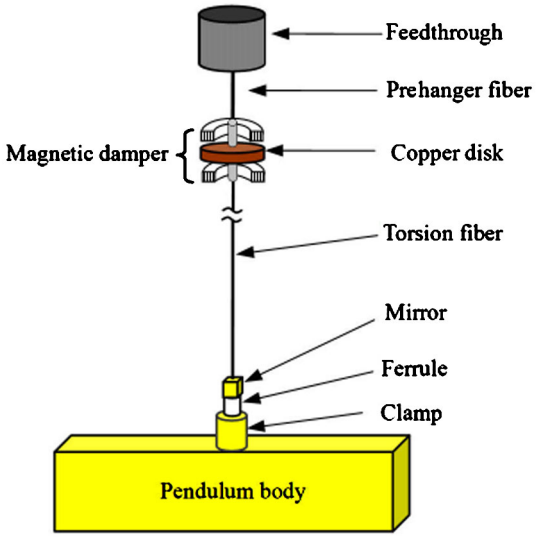

FIG. 6 (color online). Schematic diagram of the two-stage pendulum system used in both experiments I and II.

could support a 140-g load. The mass of our pendulum is less than 70 g, much lower than its elastic limit.

The fiber usually untwists at a relatively high drift rate up to 30–50 μrad/hour after it is reloaded each time. To speed up the process of the fiber's spontaneous untwisting, the fiber is heated under load to $\sim 80\,^{\circ}\mathrm{C}$ in vacuum of $\sim 1 \times 10^{-4}$ Pa for more than 36 hours and then cools down to our normal running temperature. The fiber's drift rate after heating is reduced to be less than 6 μrad/hour. Before our formal experiments, this fiber was suspended for more than two years, and the drift rate is only 2 μrad/hour and remains constant ($\pm$ 0.2 μrad) throughout our G measurements.

2. Pendulum body

The pendulum body (shown in Fig. 6) is a rectangular block made from JGS1 far UV optical quartz glass. The thermal expansion coefficient is measured to be $\alpha_p = 5.4(5) \times 10^{-7}/^{\circ}\mathrm{C}$, and the variation in temperature over the complete measurement of G is less than $0.2\,^{\circ}\mathrm{C}$. This implies that the maximum change in the pendulum's dimension is less than 0.01 μm, which is neglectable. The glass block is ground and polished with great care, and the flatness of all six surfaces is measured to be better than $\lambda/10$, where $\lambda = 632.8$ nm is the wavelength of light. The parallelism between opposite surfaces and the orthogonality between neighboring surfaces are ≤ 1 arcsec, which introduces an uncertainty of only $u_r = 0.34$ ppm to the G value.

The dimensions of the pendulum are measured by comparing it with the metrological length gauges under a commercial length comparator [45]. The gauges are calibrated by the National Institute of Metrology of China [46], and the accuracy of the measurement is $(0.03 + 0.5L/\mathrm{m})$ μm at 99% confidence level, where L is the measured length in units of meters. The systemic uncertainty of the length comparator is $(0.04 + 0.004\Delta L)$ μm, where ΔL is the length difference in units of millimeters between the measured sample and the metrological gauge used. The measured results are all converted to the values at the normal running temperature $20.20\,^{\circ}\mathrm{C}$ by

$$L_p = L_{pm}[1 + \alpha_p(20.20 - \mathcal{T})], \tag{8}$$

where L_p and L_{pm} are the lengths at $20.20\,^{\circ}\mathrm{C}$ and at the measurement temperature $\mathcal{T}$, respectively. Finally, the length, width, and height of the pendulum are determined to be 91.465 463(130), 12.014 705(52), and 26.216 178 (66) mm, respectively, at $20.20\,^{\circ}\mathrm{C}$ at 68% confidence level, and their uncertainties contribute $u_r = 1.86$, 0.54, and 0.22 ppm to the G value, respectively. The major uncertainty in length comes from the transfer of the nominal length of the gauge L_0 at its calibration temperature (usually at $20.00\,^{\circ}\mathrm{C}$) to L_p at $20.20\,^{\circ}\mathrm{C}$, owing to its thermal expansion coefficient $\alpha_g = 11.5(1.0) \times 10^{-6}/^{\circ}\mathrm{C}$ being about 20 times larger than that of the pendulum body.

The mass of the pendulum is measured by a commercial AT 106 electronic balance [47]. By using two $E2$ grade weights with masses of 10 and 50 g, the vacuum mass of the pendulum is determined to be 63.383 88(21) g after taking the air buoyancy into account. This contributes only $u_r = 0.005$ ppm to the final G value.

Three small chips are found at the sidelines of the pendulum body, which were produced during the manufacturing process. Their coordinates and dimensions are determined by using a commercial video instrument with an accuracy of 3 μm [48], and their masses are estimated by their dimensions and the density of quartz glass, as listed in Table I. Compared to the pendulum body, the chips are so small that they are all treated as negative point masses in computing corrections to $I/\Delta C_g$.

3. Density inhomogeneity

The quartz glass used consists of SiO_2 only, and its impurity content is less than 1 ppm. The empirical expression relating the refractive index n, density ρ, and chemical composition is best represented by the Gladstone-Dale relationship [49]

$$n = 1 + \chi\rho, \tag{9}$$

where χ is the specific refractivity, which depends on the chemical compositions. For the SiO_2 glass, the relationship between the mean refractive index $\bar{n}$ and the density ρ is measured to be [50] $\bar{n} = 1.032 + 0.194\rho$. Therefore, measuring changes in the refractive index over the glass block could offer information on the local density inhomogeneity of the pendulum. The density inhomogeneity of the pendulum is investigated by an optical interference method, as described in Ref. [51]. The quartz glass pendulum is placed in one optical arm of the Michelson-type interferometer and moved along one direction driven by a one-dimensional translation stage. If the pendulum's density shifted, the refractive index of the quartz glass, and in turn the interference fringe, would change correspondingly. The observed relative variations of the density over a volume with the size of $5 \times 5 \times 5$ mm^3 is $\Delta\rho/\rho = (0.99 \pm 0.92) \times 10^{-5}$. Under the assumption that the density fluctuation of the glass pendulum follows a Gaussian distribution, the density inhomogeneity of the pendulum

TABLE I. Properties of the three chips in the sidelines of the pendulum.

No.	Coordinate[a] (mm)	Mass[b] ($\times 10^{-2}$ mg)
1	45(1), 6(1), 13(1)	−2.96(1.48)
2	22(1), −6(1), −13(1)	−3.30(1.75)
3	−40(1), 6(1), −13(1)	−2.93(1.47)

[a]The origin is the GC of the pendulum.
[b]The chips are considered as negative masses in our computation.

introduces $u_r < 0.21$ ppm to the G value by performing an integral over the pendulum body.

4. Coating layer

To minimize variations of the electrostatic interaction between the torsion pendulum and its surroundings, its surface is coated with two thin metal layers by using magnetron sputtering. During the coating, the metal target is fixed and the sample is rotated at the rate of ~20 turns per minute. A copper sublayer of 99.999% purity is coated to acquire better adhesion, and the surface layer is coated with gold of 99.999% to act as a conductive material. The gold layer has a small variation in the work function due to its different crystal faces [2]. The mass of the coating layers, determined from the mass difference before and after coating, is 49.863(26) mg, and the combined density of the coating layers is estimated to be 15.83(1.00) g/cm^3.

An identical pendulum coated with the same process is used to investigate the inhomogeneity of the coating layer [52]. This pendulum is cut into 19 small blocks along the length, shown in Fig. 7. The average thickness of the coating layer is determined by comparing the mass changes of the blocks at different positions on the pendulum before and after coating, where the coating area of each small block is measured by the video instrument [48]. The coating and measurements are repeated twice for each pair of surfaces. During each coating, one of the end surfaces is coated, the coating thickness of which is chosen as the reference. The statistical results reveal that the thickness of the coating layer is almost uniform on each surface but varies for different surfaces, as shown in Fig. 8. The measured average thickness ratio of the lateral (large) to the end surface (the reference) is 0.824(41), and that of the bottom surface to the end surface is 0.782(23). Because

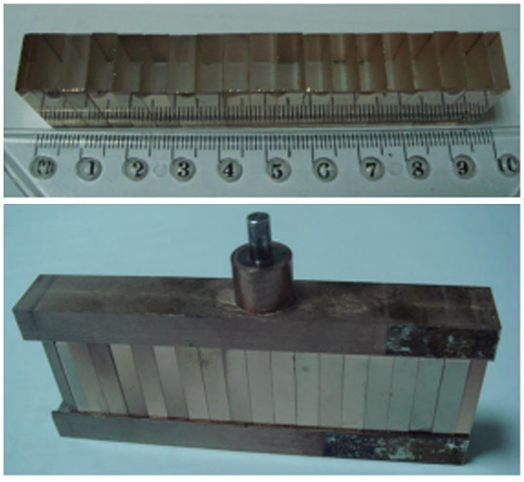

FIG. 7 (color online). Top: The pendulum is cut into 19 blocks to investigate the inhomogeneity of the coating layer. Bottom: The 19 blocks are assembled and the lateral (large) surfaces are coated.

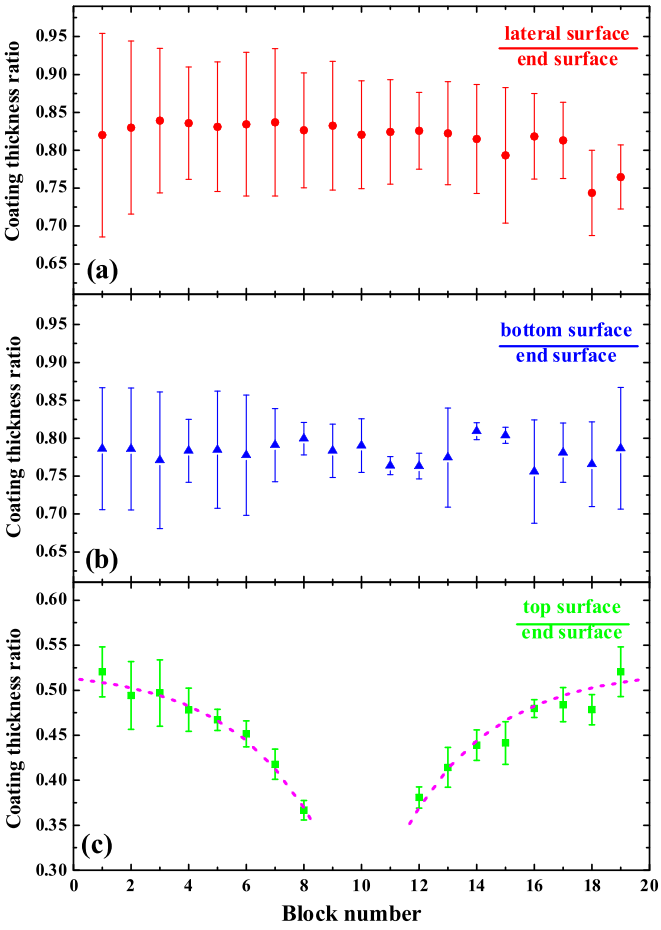

FIG. 8 (color online). The measured coating thickness ratio of (a) the lateral, (b) bottom, and (c) top surfaces to the reference thickness for 19 small blocks. Because of the presence of the aluminum clamp, the coating thickness on the top surface of the pendulum takes on a symmetric exponential distribution along the length, and the dashed lines show the least-square fits.

of the presence of the aluminum clamp attached to the center of the top surface, as shown in Fig. 6, the thickness ratio takes a symmetrical exponential distribution $h(x) = 0.52(1) - 0.30(3)e^{-x/14.6(3.2)\ \mathrm{mm}}$, where x is the distance from the center to the end surface.

From the measured thickness ratios and the total mass, the thickness of the coating layers can be found. They contribute a downward correction of 24.28(4.33) ppm to our final G value. If the thickness distribution were uniform, its correction would be only 2.7 ppm.

5. Clamp and ferrule

The aluminum clamp with a mass of 3.469 612(4) g consists of two parts. The bottom part is a cylinder with a diameter of 12.036(6) mm and a height of 10.133(7) mm, and the top part is a 1:50 circular cone with a bottom diameter of 4.010(22) mm and a height of 7.798(7) mm, as shown in Fig. 9. The clamp is glued to the center of the pendulum's upper surface. The mass of the glue is 1.821

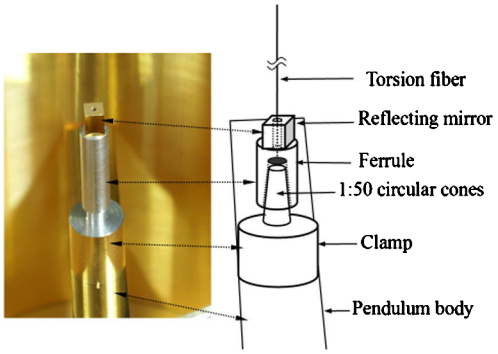

FIG. 9 (color online). Schematic diagram of the clamp and ferrule used to connect the pendulum to the torsion fiber. The inset shows a closeup photo of the suspended pendulum surrounded by the hollow gold-coated aluminum cylinder.

(17) mg, and the thickness is 13.3(2.2) μm. The deviations between the clamp and the pendulum are measured to be 0.015(4) and 0.016(4) mm in the X and Y directions, respectively.

The cylindrical aluminum ferrule has a mass of 0.773653(4) g, an outer diameter of 6.096(6) mm, and a height of 15.096(7) mm. At the bottom of the ferrule, there is a 1:50 circular cone with a diameter of 4.040(14) mm and a height of 12.336(53) mm, which fits with the clamp tightly. On the top, a small 0.6(1)-mm-diameter hole is drilled through the center to pass the torsion fiber. Epoxy is used to fix the torsion fiber by filling the small hole and the space above the circular cone.

6. Mirror

The gold-coated mirror is a cubical K9 glass with outer dimensions of $4.079(3) \times 4.071(13) \times 4.053(16)$ mm^3 and a mass of 158.4937(37) mg, and a hole with a diameter of 1.177(8) mm is drilled through the center to pass the torsion fiber, as shown in Fig. 9. The mirror is glued to the center of the ferrule and used to reflect the laser beam, which monitors the pendulum twist.

7. Magnetic damper

The passive magnetic damper is used to suppress the unwanted modes of the torsion pendulum [35–37]. A ring

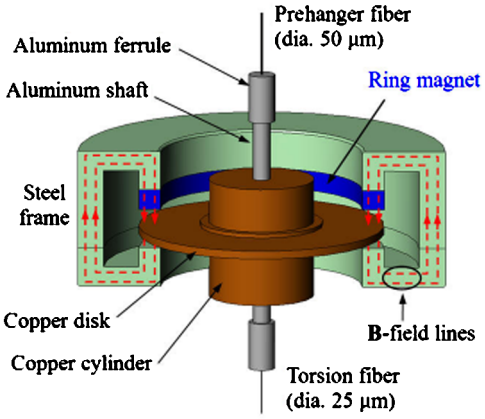

FIG. 10 (color online). Cross section of the magnetic damper used in our G measurement. The circularly symmetric copper disk suspended in the **B** field suppresses the swing, guitar-string, and wobble modes of the pendulum but has a negligible effect on the damping of the torsional mode.

magnet (shown in Fig. 10), enclosed by two steel frames, produces a **B** field in the region where the copper disk is suspended. Because of the damper's axial symmetry, the **B** field suppresses only the swing, guitar-string, and wobble modes of the pendulum efficiently, while having a negligible effect on the damping of the torsional mode. A typical exponential damping time of such unwanted modes is now several torsional periods.

Because of the existence of the magnetic damper, the frequency of the torsion pendulum without the source masses is modified to [53]

$$\omega_0^2 = \frac{IK + I_mK + IK_m}{2I_mI} - \frac{\sqrt{(IK + I_mK + IK_m)^2 - 4I_mIK_mK}}{2I_mI}, \quad (10)$$

where I, I_m, K, and K_m have been defined in Fig. 2. When the pair of source masses is positioned in their expected positions at the opposite sides of the pendulum, an effective gravitational spring constant K_g produced by the source masses shifts the pendulum's frequency to

$$\omega^2 = \frac{IK + I_mK + IK_m + I_mK_g}{2I_mI} - \frac{\sqrt{(IK + I_mK + IK_m + I_mK_g)^2 - 4I_mI(K_mK + K_gK_m + K_gK)}}{2I_mI}. \quad (11)$$

According to Eq. (7), the correction to G due to the magnetic damper is

$$\frac{\Delta G}{G} = -\frac{I_mK^2}{IK_m^2}. \quad (12)$$

The total mass of the copper disk and cylinder, as well as the aluminum shaft, is 111.9050(10) g, and the moment of inertia of the magnetic damper is measured to be $I_m = 2.220(18) \times 10^{-5}$ kg m^2. By suspending a disk pendulum with the moment of inertia equal to that of the magnetic

damper but the mass equal to the total mass of the two-stage pendulum in the G measurement, and measuring the period of free oscillation, the torsion constant of the pre-hanger fiber is determined to be $K_m = 1.048(9) \times 10^{-6}$ N m/rad.

The moment of inertia of the pendulum is calculated to be $I = 4.5057(1) \times 10^{-5}$ kg m^2. The free oscillation of the two-stage pendulum system, monitored for about 67 hours, yields a free oscillation period of $T_0 = 2\pi/\omega_0 = 535.01(2)$ s. By using Eq. (10), the torsion constant of the torsion fiber is calculated to be $K = 6.2516(5) \times 10^{-6}$ N m/rad. Substituting these parameters into Eq. (12), we obtain a correction of 17.54(31) ppm to G due to the magnetic damper.

D. The source masses

The pair of spherical source masses was made of 316 stainless steel [54]. Ten spheres with initial nonsphericity of ~ 5 μm were ground and polished by hand over a two-year period with great care (Fig. 11). Finally, four of them achieved a nonsphericity of better than 0.3 μm. They are numbered as spheres 1–4. Spheres 2 and 4 have mass and diameter more closely matched and hence were chosen as the source masses in our G measurement. Compared to the cylindrical source masses used in HUST-99 [28], the spherical source masses have the following advantages: (i) a sphere has global symmetry while a cylinder has only an axial symmetry, which in principle permits us to change the orientation of the source mass arbitrarily to average out density fluctuations and nonsphericity; (ii) the offset of the CM from the GC is found to be much smaller than that of the cylinder, which reveals that the density is more homogeneous. In this section, we describe the measurements of the masses, diameters, sphericities, offsets of the CM from the GC, density inhomogeneity, and magnetic properties of the source masses.

1. Masses

The masses of the spheres are measured by a commercial electronic balance (PR-2004) [55] with a resolution of 0.1 mg and an accuracy of 0.8 mg. The readout M_0 of this balance should be corrected due to the air buoyancy to find the vacuum mass M, by using the relationship

$$M_0 = M\frac{1-\frac{\rho_k}{\rho}}{1-\frac{1.2}{8000}} = \frac{M-\rho_k V}{1-\frac{1.2}{8000}}, \tag{13}$$

where ρ and V are the density and volume of the sphere, respectively, and the air density is $\rho_k \approx 1.2$ kg/m^3. Because ρ_k is time-varying and difficult to measure precisely, the vacuum mass of another sphere, whose volume is almost the same as that of spheres 2 and 4, is determined by a vacuum balance in National Institute of Metrology of China. The measured value, $M_s = 779.309\,37(1)$ g, serves as a reference for determining the vacuum masses of spheres 2 and 4 by the relationship

$$M = M_s + \left(1-\frac{1.2}{8000}\right)\Delta M - \rho_k \Delta V, \tag{14}$$

where ΔM and ΔV are the differences in mass and volume between sphere 2 (or 4) and the reference, respectively.

The masses are weighed in the sequence of $A - B_2 - B_4 - A - \ldots$, where A, B_2, and B_4 denote the reference sphere, sphere 2, and sphere 4, respectively. After repeating the measurements for 6 [12] times in experiment I [II], the net differences ΔM of spheres 2 and 4 are determined to be $-1.130\,15$ [$-1.129\,90$] and $-1.133\,20$ [$-1.133\,90$] g with uncertainties of 0.24 [0.09] mg and 0.19 [0.10] mg, respectively. The last term in Eq. (14) becomes $\rho_k \Delta V = 0.17$ mg, which is only one-fifth of the accuracy of the electronic balance and is regarded as a systematic error. Finally, the vacuum masses of spheres 2 and 4 are determined to be 778.1794(9) [778.1796(9)] and 778.1763(9) [778.1756(9)] g in experiment I [II], respectively, and each one contributes an uncertainty of $u_r = 0.58$ ppm to the final G value.

2. Diameters

The diameters of the spheres are determined by an improved rotating gauge method [56,57]. Three spheres are placed in a horizontal line (Fig. 12), and then the three surface separations (S_{12}, S_{23}, and S_{13}) are measured indi-

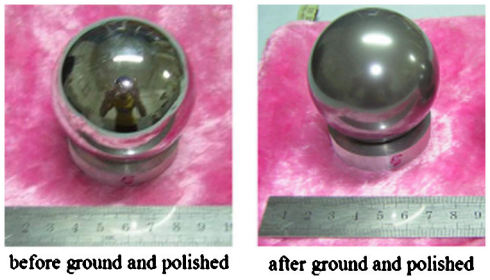

FIG. 11 (color online). Photograph of a spherical source mass used in our G measurement. After grinding and polishing by hand, the nonsphericity of the sphere is improved from ~ 5 μm to less than 0.3 μm.

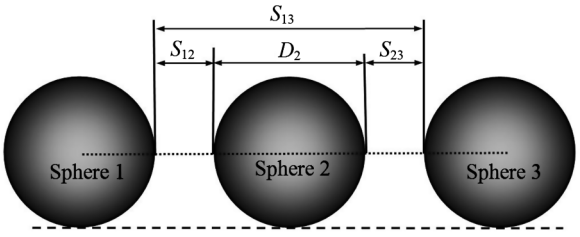

FIG. 12. Schematic diagram for measuring the diameter of sphere 2 (front view). S_{12}, S_{23}, and S_{13} denote the surface separations. Since the three spheres form a horizontal line, ideally, $D_2 = S_{13} - S_{12} - S_{23}$.

vidually. The diameter of the middle sphere is determined ideally by

$$D_2 = S_{13} - S_{12} - S_{23}. \tag{15}$$

Figure 13 shows a schematic diagram for determining the surface separation S_{13}. Spheres 1 and 3 are supported by two Zerodur rings that are mounted on a large Zerodur disk. A 100.000 14(3)-mm-long gauge block [46], which is slightly shorter than the gap between the two spheres, is hung from a 100-μm-diameter and 70-mm-long tungsten fiber. The top end of the fiber is attached to the stepper motor, which is mounted on a steel frame by a two-dimensional translation stage. A mirror adhered onto the gauge block is used to monitor the rotation of the gauge. The stepper motor is remotely driven by a computer via a digital-to-analog converter. The heat produced by the stepper motor is isolated by surrounding the spheres and the gauge with a small foam box (not shown in Fig. 13).

The rotation angle of the gauge block is continuously monitored by a commercial electronic autocollimator (Vario 140/40) [58], and the temperature changes of the spheres and the gauge block are simultaneously monitored by three temperature sensors with an accuracy of 0.01 °C. At each position of the gauge block touching the spheres, the motor is kept still for ~240 s. One typical data set for the rotation angle measured as a function of time is shown in Fig. 14. The surface separation calculated is plotted in Fig. 15, in which the recorded outputs of the two temperature sensors are averaged over a duration of 240 s to correct for the thermal effect. The scatters of the data points in Fig. 15 are mainly due to nonrepeatability of measurements of the contact points. The statistical error is reduced by averaging. However, the error bars on the individual data points represent systematic errors, which are not averaged out.

After the gap S_{13} is measured, the long gauge block is removed and sphere 2 is placed between spheres 1 and 3. Two short gauges with lengths of 21.425 040(15) and 21.425 100(15) mm [59] are separately suspended to measure the two small gaps S_{12} and S_{23}. After one set of S_{12} and S_{23} is determined, we can calculate a value for the diameter of sphere 2. In practice, the diameter is calculated from (a detailed derivation is given in Appendix C)

$$D_2 = \frac{S^r_{13}}{2}\left[\frac{1}{\cos\beta_{12}\cos\gamma_{12}} + \frac{1}{\cos\beta_{23}\cos\gamma_{23}}\right] - S^r_{12} - S^r_{23}, \tag{16}$$

where S^r_{ij} is the surface separation between spheres i and j at the reference temperature $\mathcal{T}_r$, and γ_{ij} and β_{ij} are the angular deviations denoting that the three center lines of each pair of spheres are not collinear in the horizontal and vertical planes, respectively. After one value of the diameter is obtained, the orientation of sphere 2 is changed and the measurements of S_{12} and S_{23} are repeated. For each sphere, ten sets of measurements are obtained to average out the nonsphericity. In the end, sphere 2 is removed and

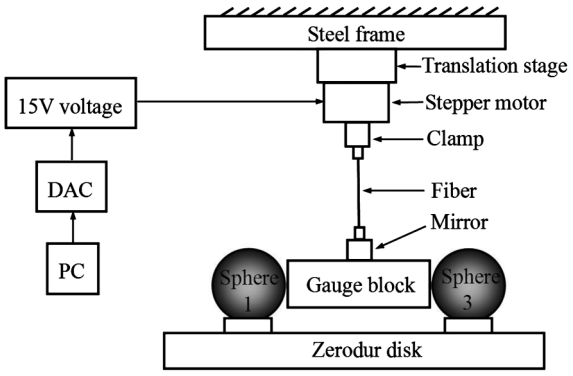

FIG. 13. Schematic setup for determining the surface separation S_{13}.

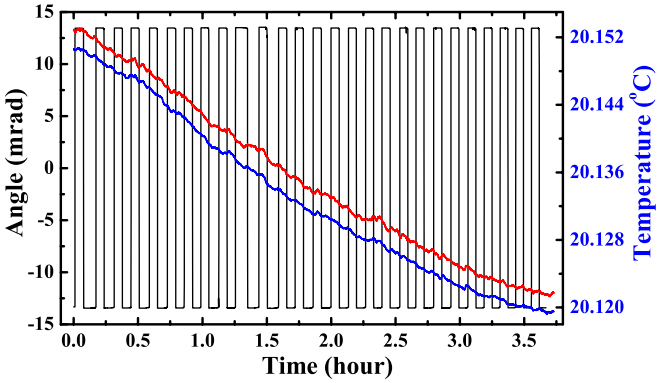

FIG. 14 (color online). Typical data set for the rotation angle of the gauge block and the recorded outputs of the two temperature sensors in measuring S_{13}. At each contact position, the motor is kept still for ~240 s and then is rotated to the other contact position.

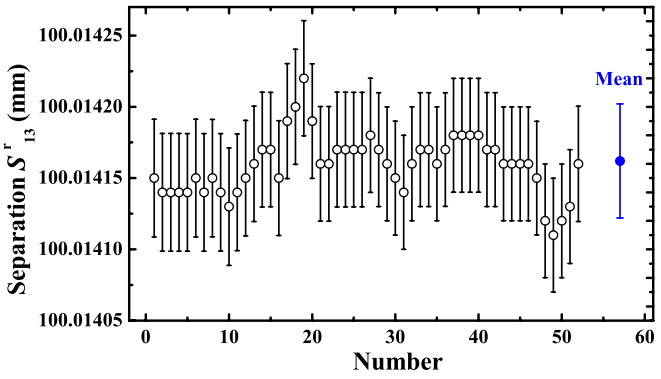

FIG. 15 (color online). Measured separations S_{13} according to the data of Fig. 14. Each hollow circle represents one separation deduced from one time of changing the contact position, and the error bars are the systematic uncertainty. The scatter of the plotted data is due to the fluctuation of the rotation angle mainly, which shows the varied condition of contact position during measurements. The last solid circle is the mean.

S_{13} is measured again to confirm the positions of spheres 1 and 3 being unchanged.

Ten sets of the measured diameters for spheres 2 and 4 are shown in Fig. 16. The hollow circles represent the diameter in different orientations, and the solid circles are the average values. Nonsphericity of the spheres apparently causes deviations of the individual measurements from the average values. The diameters of spheres 2 and 4, converted to the corresponding values at the reference temperature $\mathcal{T}_r = 20.20\,^{\circ}\mathrm{C}$, are determined to be 57.151 01(26) [57.151 23(30)] and 57.150 63(29) [57.150 74(31)] mm in experiment I [II], respectively. The error budget in measuring the diameter of sphere 2 is listed in Table II. The major error source is the nonsphericity, which is discussed in the following section.

3. Sphericities

Nonsphericity constitutes the dominant error source in determining the diameters of the spheres. We used a commercial sphericity measuring instrument [60] with an accuracy of 0.03 μm to measure the sphericity of the source masses. A standard ellipsoid ring with a sphericity of 4.43 μm [61] is used to calibrate the instrument before and after the sphericity measurements. For each sphere, over 25 different scans are performed in different orientations. A typical scan of sphere 2 is shown in Fig. 17, which gives a sphericity of 0.178 μm after least-square fitting.

The sphericities of spheres 2 and 4 are determined by averaging all the values scanned in different orientations, as shown in Fig. 18. The resulting sphericities for spheres 2 and 4 are 0.23(3) and 0.27(9) μm, respectively.

TABLE II. Error budget in determining the diameter D_2 according to Eq. (16) in experiment II.

Error sources	Uncertainty (μm)
Surface separation S_{13}^r	0.11
Surface separation S_{12}^r	0.04
Surface separation S_{23}^r	0.04
Angular deviations	<0.01
Nonsphericity	0.23
Statistical error	0.15
Total	0.30

4. CM offsets

The offsets of the CM from the GC of the spheres are measured by a weighbridge method [62] using the commercial PR 2004 electronic balance [55]. We use the Zerodur glass to assemble the weighbridge to lower the effect of environmental temperature fluctuation. As shown in Fig. 19, a 200-mm-long, 60-mm-wide, 8-mm-thick Zerodur block is used as a horizontal bridge. One end of the bridge stands on the tray of the electronic balance by one pivot in the middle, and the other end stands on a 100-mm-diameter Zerodur cylinder from two pivots. A Zerodur ring is mounted on the weighbridge for locating the sphere. The CM and GC of the sphere are denoted by S and O in Fig. 19, respectively. If the CM and GC were not coincident, rotating the sphere around the vertical axis would lead to a changing readout of the electronic balance.

Before each measurement, the balance is calibrated by a standard weight and the output is reset to zero. The sphere is then put on the Zerodur ring and the orientation of the

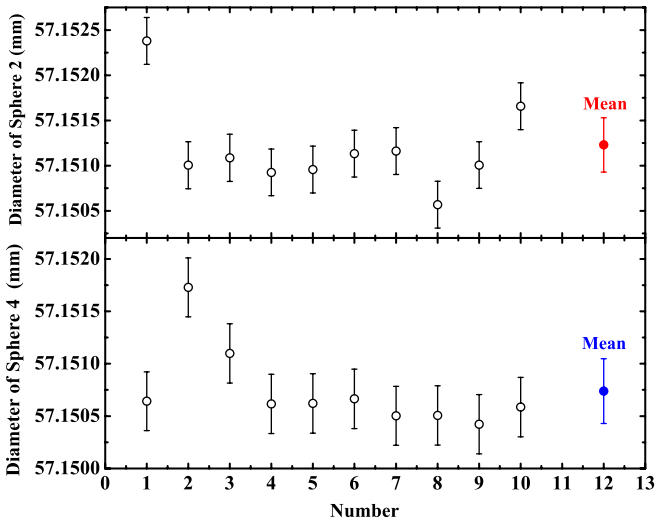

FIG. 16 (color online). The diameters of spheres 2 (upper) and 4 (lower) determined by the improved rotating gauge method. Each hollow circle denotes the measured diameter in different orientations, and the last solid circle is the statistical average.

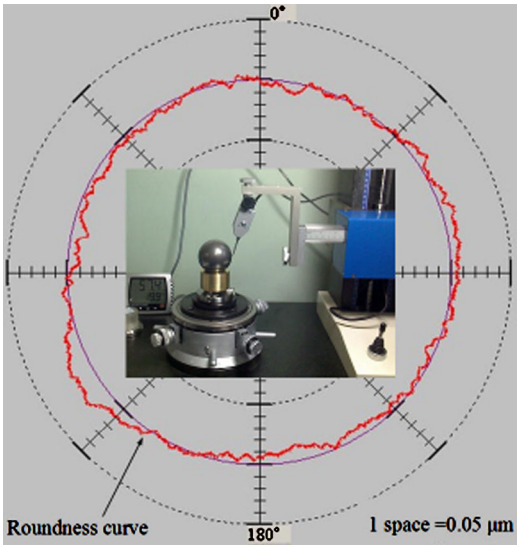

FIG. 17 (color online). Typical roundness curve of sphere 2 scanned by the sphericity measuring instrument. Each space is 0.05 μm. This curve corresponds to a sphericity of 0.178 μm. The inset photo shows the sphere on the sphericity measuring instrument.

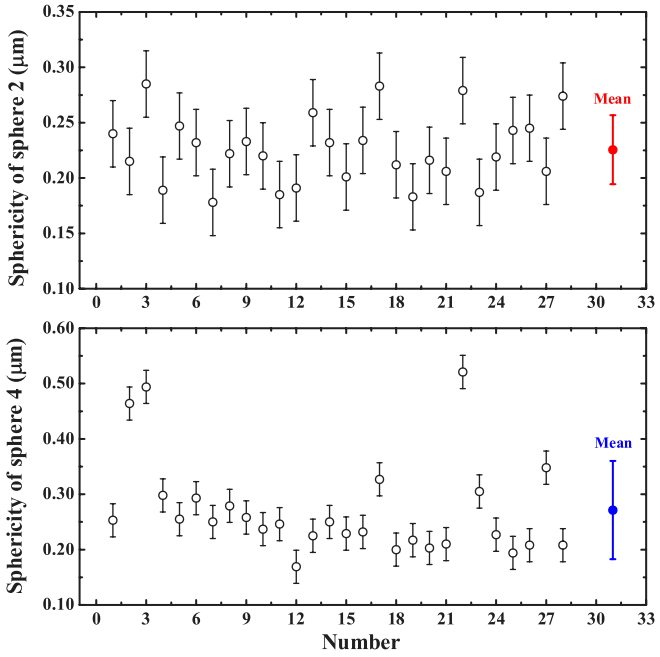

FIG. 18 (color online). The measured sphericities of spheres 2 (upper) and 4 (lower) in different orientations. Each measurement has an error of ~0.03 μm, and the sphericity of sphere 4 is more dispersive than that of sphere 2. Each solid circle is the statistical average over all the measured sphericities for each sphere.

sphere is changed by rotating the sphere about the Z axis with an incremental step of 22.5°. The reading of the balance M varies with the sphere's azimuth as

$$M = \frac{L_g - e\sin\theta\sin\varphi}{L} M_0, \tag{17}$$

where L is the effective span of the weighbridge, L_g is the horizontal distance from the right pivots to the GC, the CM offset of the sphere e is equal to the length of the line OS, θ is the angle between the line OS and the Z axis, φ is the angle between the projection of OS onto the XY plane and the X axis, and M_0 is the mass of the sphere. For each full circle about the Z axis, the maximum and minimum outputs of the electronic balance are, respectively,

$$M_{\max} = \frac{L_g + e\sin\theta}{L} M_0, \qquad M_{\min} = \frac{L_g - e\sin\theta}{L} M_0. \tag{18}$$

The Z component of the offset e_z can be written as

$$e_z = e\sin\theta = \frac{M_{\max} - M_{\min}}{2M_0} L. \tag{19}$$

By using the same method, we obtain the components e_x and e_y. Then, e is calculated from

$$e = \sqrt{\frac{e_z^2 + e_x^2 + e_y^2}{2}}. \tag{20}$$

A typical variation of the weighbridge output as a function of the azimuth rotated is shown in Fig. 20. For each axis, the measurement is repeated for more than five turns to average out the nonsphericity of the spheres. We use a sine function to fit the data and obtain the components e_x, e_y, and e_z. We find that the total CM offsets of spheres 2 and 4 are 0.34(8) and 0.24(8) μm, respectively.

In HUST-99 [28], the axial CM offsets of the two cylindric source masses used were found to be 10.3(2.6) and 6.3(3.7) μm, which resulted in a 210-ppm correction to the original HUST-99 value of G with an uncertainty of $u_r = 78$ ppm. The CM offsets of the spheres are a factor of more than 19 smaller than those of the cylinders, and the measured values are limited principally by the nonsphericity of the spheres. This reveals that the density homoge-

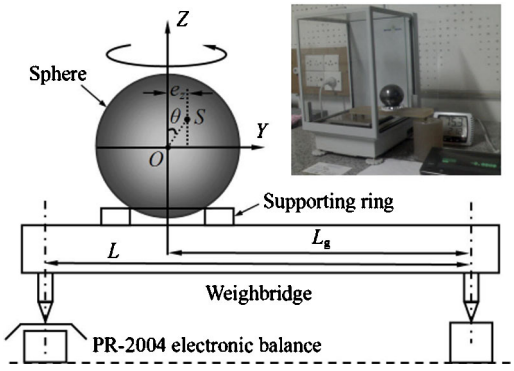

FIG. 19 (color online). Schematic diagram for determining the CM offset of the sphere. The Zerodur weighbridge with an effective span of L is supported by three pivots: one is centered on the tray of the balance, and other two are supported by a Zerodur cylinder. The sphere is positioned on a Zerodur ring mounted on the weighbridge and is rotated about the vertical axis by hand. The inset is the photograph of the weighbridge.

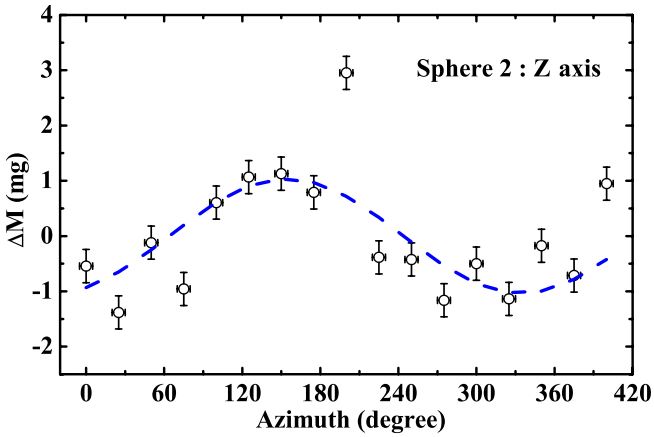

FIG. 20 (color online). Typical data of the weighbridge output versus the azimuth in measuring the Z component of CM offset e_z for sphere 2. Sphere 2 is rotated about the Z axis by 22.5° per step. The dashed line shows the fit to a sine function.

neity of the spheres used in these experiments is much better than that of the cylinders used in HUST-99.

5. Density inhomogeneity

The density inhomogeneity of the spheres is investigated by using two different methods: (i) measuring the CM offsets of the spheres (as discussed above) and (ii) scanning the internal disfigurement with a scanning electron microscope (SEM) [63], in which the density inhomogeneity of the spherical source mass is determined by the backscattered electron images.

One of the spheres from the same batch is cut into seven rectangular blocks with dimensions of $23 \times 23 \times 5$ mm^3, as shown in Fig. 21. Out of the seven specimens, one is cut from the center of the sphere and the other six are cut along six different directions of the sphere. The disfigurement on the specimen surfaces, prepared by grinding and polishing, is scanned by the SEM.

The microscope is operated at an accelerating voltage of 20 kV, and the working distance is about 12.4 mm. The backscattered electron images are captured from the randomly selected regions at a nominal magnification of 500. The scanned region is about 0.272×0.234 mm^2, and hence many scanned regions can be selected from one prepared specimen. To ensure that the selected specimen regions adequately reflect the general density distribution of the sphere, 30 scanned regions are randomly selected from each specimen and examined under the same brightness and contrast conditions. Hence, there are altogether 210 samples selected from the seven specimens in our test.

Analyzing all 210 digital images, we obtain a relative density inhomogeneity of the sphere better than 5.9×10^{-4} over a volume of $0.272 \times 0.234 \times 0.005$ mm^3. If we assume that the density inhomogeneity of the spheres used in our G measurement is the same as that of the sample sphere, it should contribute an uncertainty of less than 0.03 ppm to the G value [64].

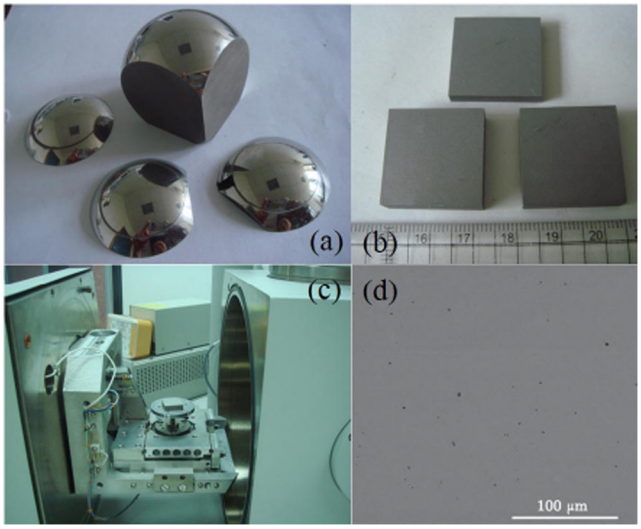

FIG. 21 (color online). (a) A cut stainless steel sphere. (b) Three specimens. (c) One specimen is put on the platform of the FEI-Quanta 200 SEM. (d) A typical microscope image. The largest black region against the gray background is about 5 μm in diameter.

The disadvantage of this method is that the sphere is demolished in the measurement process. In our experiment, the positions and orientations of the two source masses are exchanged in experiment II, and the G measurement is repeated independently. As presented in Sec. VI, the difference in the two G values obtained in experiments I and II is only 9 ppm, and half of this discrepancy is attributed to the density inhomogeneity.

6. Magnetic property

In the time-of-swing method, the constant component of the local magnetic field is canceled between the near and far positions, but the time-varying part will introduce an equivalent magnetic spring constant K_B, just like the gravitational spring constant K_g due to the spheres.

We chose SS316 for the source spheres because it is the least magnetic in all stainless steel. The variation of the magnetic field is investigated by placing a commercial three-axis magnetometer (with a resolution of 0.01 mGs) [65] at the normal location of the pendulum. The near and far positions are switched by rotating the turntable by $\pm 90°$ at intervals of 10 minutes, and no change is observed at the resolution of 0.01 mGs. To investigate the gradient of the local magnetic field, the magnetometer sensor is placed in the different regions to be occupied by the suspended pendulum, and still no change is observable. The effect of the magnetic field modulated by a pair of coils on our G measurement will be discussed in Sec. IV D.

E. Alignment and positioning

The relative positions between the pendulum and the source masses are used to calculate the gravitational couplings C_{gn} and C_{gf} in Eqs. (4) and (5) and to determine ΔC_g in Eq. (7). For a precise alignment of the pendulum with respect to the source masses, first, a Zerodur disk is mounted on the leveled turntable (see Fig. 3), and the pair of the source masses is mounted symmetrically centered on the turntable. Their surface separation is measured with the rotating gauge method described in Sec. II D 2. The torsion fiber is then aligned with the rotation axis of the turntable, and the attitude and position of the pendulum are measured. Subsequently, the angle between the center line of the source masses and the equilibrium direction of the pendulum is determined and then adjusted to zero. Finally, a thin hollow aluminum cylinder acting as an electrostatic shield is inserted to surround the pendulum. The following subsections will discuss the methods of assembly and measurements in detail.

1. Turntable

The switching between the near and far positions is performed by a commercial model 410 turntable with the minimal increment of 0.0005°/step [39], and the nominal resolution and accuracy are 0.18 and <30 arcsec, respectively. The turntable is mounted on the lower floor of the chamber by three pairs of screws. The Zerodur disk with a diameter of 240(1) mm and thickness of 25(1) mm is embedded into the circular groove of an aluminum plate fixed on the turntable. The two surfaces of the Zerodur disk are polished to a flatness of <5 μm. The level of the Zerodur disk is monitored by a level gauge with a resolution of 20 μrad and is carefully adjusted to within that resolution by using the three pairs of screws. Because of the extremely low thermal expansion coefficient of the Zerodur disk, $0(1) \times 10^{-7}/°\mathrm{C}$, its upper surface is chosen as the horizontal reference in determining the relative heights of the pendulum and source masses.

The turntable is driven by a stepper motor through 360:1 reduction gearing. The reversal interval of the turntable is measured as follows: a mirror is attached to the turntable, and an autocollimator is used to monitor the rotation of the turntable. The turntable is rotated at a step of 0.2° per 180 s. After three steps, the rotation direction is reversed, and the measurement is repeated. The recorded angle versus time is shown in Fig. 22. The rotation direction is reversed 12 times, and the 12 reversal intervals are averaged to be 0.0018(5)°. The mean value for 25 sets of 0.2° step without the reversal interval is found to be 0.2000(5)°, well consistent with the nominal value of the turntable.

We randomly chose several different positions and different rotation steps to perform the same measurements and found almost the same results. With the assumption that the reversal interval is independent of the rotation angle, it is used to correct the ±90° angle of switching between the near and far positions.

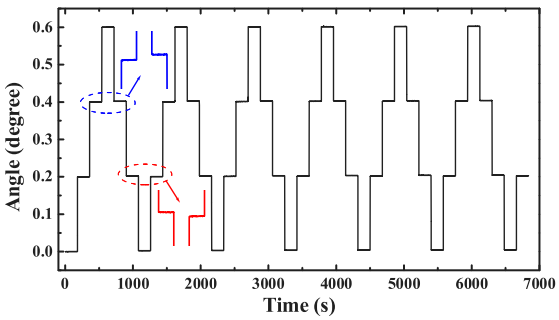

FIG. 22 (color online). Rotation angle versus time in measuring the reversal interval of the turntable. The turntable is rotated at a step of 0.2° per 180 s. After three steps, the rotation direction is reversed and the reversal interval appears, as the enlarged insets show there.

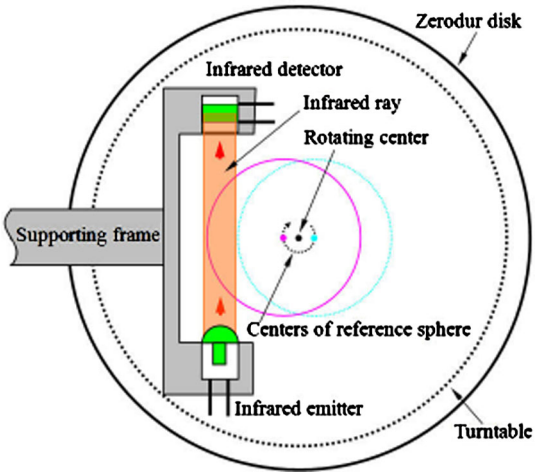

FIG. 23 (color online). Schematic diagram (top view) for finding the rotation center of the Zerodur disk, which is mounted on the turntable. The infrared emitter and detector are fixed to a platform free from the turntable. If the reference sphere is not at the rotation center, the motion of the reference sphere modulates the flux of the infrared ray as the turntable rotates.

2. Positioning the source masses

The positioning process is carried out as follows. First, the rotation center of the Zerodur disk is determined by using a reference sphere with the same dimension as that of the source masses with the help of an infrared detector fixed independent of the turntable. Initially, the reference sphere, supported by a Zerodur ring, is placed approximately at the center of the Zerodur disk, as shown in Fig. 23. The turntable is rotated and the output of the infrared detector is recorded. A modulation of the infrared flux indicates a deviation of the reference sphere from the true center of the turntable. Then, the reference sphere is moved to reduce the modulation amplitude. This process is repeated until there is no obvious variation in the output of the infrared detector. The supporting ring under the reference sphere is then glued onto the Zerodur disk.

Figure 24 shows the outputs of the infrared detector versus the angle of the turntable at two stages of adjustment. The dashed line is the result at an interim stage, which shows that the reference sphere is off from the center of the turntable by about 4 μm. The solid line shows the final result obtained in our G measurement, which gives a deviation of less than 2 μm.

After the rotation center of the Zerodur disk is located, spheres 2 and 4, supported by Zerodur rings 2 and 4, respectively, are put on the Zerodur disk in line with the reference sphere with the help of two long parallel glass rulers (with a surface flatness of <0.1 μm, an orthogonality of <1 arcsec, and a parallelism of <1 arcsec. All the glass rulers and gauges used in our G measurements are ground and polished under this criterion). The separations between the two adjacent spheres are controlled by two other 21.430-mm-long gauges, as shown in the top drawing

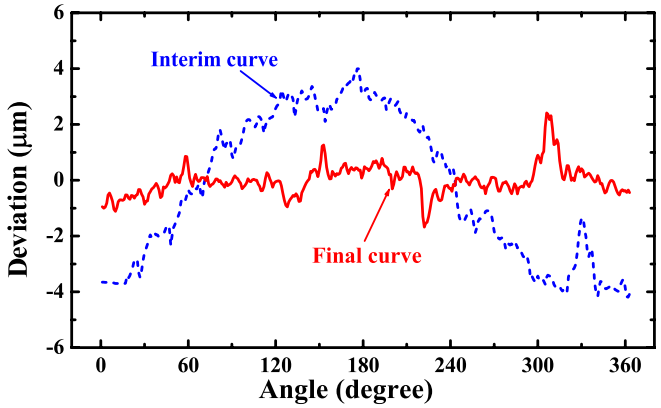

FIG. 24 (color online). Measurement of the center deviation between the reference sphere and the turntable. The dashed line shows the result of an interim adjustment, and the solid line is the final result, which gives the center deviations of 4 and 2 μm, respectively.

of Fig. 25. Zerodur rings 2 and 4 are then glued onto the Zerodur disk. Considering all the metrology errors, the center deviation between the reference sphere and the turntable, differences in the diameters of the three spheres, and difference in the lengths of the two 21.430-mm-long gauges, we find that the centers of the source masses (spheres 2 and 4) are off from the rotation axis by no more than 3 μm. These contribute only $u_r = 0.01$ ppm to the G value.

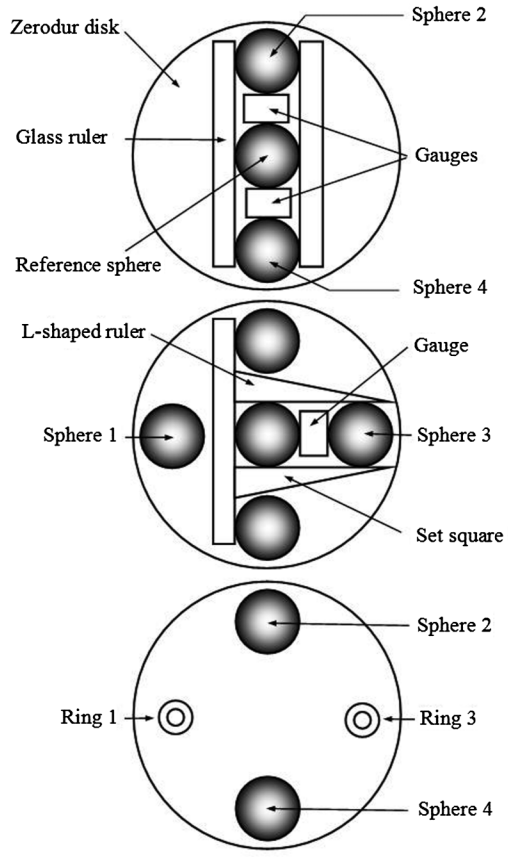

FIG. 25. Schematic diagrams (top view) for positioning the source masses and the supporting rings onto the Zerodur disk. Top: Positioning spheres 2 and 4 and their supporting rings. Middle: Locating counterbalancing rings 1 and 3. Bottom: Only spheres 2 and 4 supported by rings 2 and 4, and counterbalancing rings 1 and 3 remain.

In order to balance the gravitational torque due to supporting rings 2 and 4, two identical Zerodur rings 1 and 3 are positioned at the orthogonal locations with respect to rings 2 and 4. As shown in the middle drawing of Fig. 25, by using two L-shaped rulers, a 21.430-mm-long gauge, and sphere 3, ring 3 is located and glued to the Zerodur disk. Ring 1 is located and glued to the Zerodur disk with the same method. Finally, the reference sphere, its supporting ring, and spheres 1 and 3 are taken away, leaving only the four Zerodur rings and the pair of source masses, as shown in the lower drawing of Fig. 25. The detailed dimensions and masses of the four Zerodur rings are listed in Table III.

3. Distance between the centers of the source masses

The distance between the centers of the source masses is one of the key factors in our experiments, which is composed of the surface separation and the two radii of the source masses. In experiment I, the surface separation is determined to be 100.010 720(80) mm at 20.20 °C by using the rotating gauge method, as discussed in Sec. II D 2. In experiment II, the positions of the two spheres are exchanged, and the orientations of the source masses relative to the pendulum are changed randomly. The surface separation is determined to be 100.219 124(95) mm, which is larger than that in experiment I by about 209 μm, and is mainly due to the aluminum foil covering on the Zerodur supporting rings.

From the determined surface separations and the diameters of the source masses as found in Sec. II D 2, the distance between the centers of the source masses is calculated to be 157.161 54 [157.370 11] mm in experiment I [II]. The uncertainty of the distance consists of three parts: the uncertainties of the diameters (Sec. II D 2), the measured nonsphericities of the source masses (Sec. II D 3), and the uncertainty of the surface separation. The three parts are added quadratically and yield an uncertainty of 0.37 μm for experiments I and II, which contribute $u_r = 9.6$ ppm to the G value in both experiments. This is the largest uncertainty in our G measurement caused by the

TABLE III. Parameters of the four Zerodur rings.

Ring	Mass (g)	Inner diameter (mm)	Height (mm)
1	36.0798(10)	30.375(2)	10.003(6)
2	35.6695(10)	30.448(2)	10.004(6)
3	36.2833(10)	30.410(2)	10.003(6)
4	35.6515(10)	30.382(7)	10.002(6)

geometrical metrology error and density inhomogeneity of the masses.

4. Center height of the source masses

The center height of the sphere with respect to the Zerodur disk is measured directly by using two bridges, which consist of four glass gauges, as shown in Fig. 26. Two of the three glass gauges ($H_1 < H_2 < H_3$) with a height difference of 10(1) μm are placed on the opposite sides of the sphere symmetrically, and a long horizontal glass gauge is freely set on the two vertical glass gauges. If there is a gap between the horizontal gauge and the right vertical gauge, the horizontal gauge will rattle when it is pressed. This means that the distance from the top of the sphere to the Zerodur disk is higher than $(H_1 + H_2)/2$ but lower than $(H_2 + H_3)/2$. The Zerodur disk is chosen as the horizontal reference, and the center heights of spheres 2 and 4 are determined to be 34.176(6) [34.229(7)] and 34.188(6) [34.218(6)] mm in experiment I [II], respectively, where the difference between the two experiments is attributed to the aluminum foil on the Zerodur supporting rings.

5. Alignment with fiber

To align the rotation axis of the turntable to the torsion fiber, the turntable is adjusted by two micrometers, which are mounted perpendicularly on the bottom of the vacuum chamber. The infrared detector discussed above is fixed on the turntable, which monitors the excursion of the cylindrical clamp at the top of the pendulum from the rotation axis of the turntable. The torsion fiber is so thin that it cannot be monitored by the infrared detector directly. Because the torsion fiber may not be at the center of the clamp, the alignment is divided into two steps, as shown in Fig. 27.

The first step is rotating the turntable (and the infrared detector) around the clamp by one turn. By using the output of the infrared detector at four edges 1–4, the rotation axis of the turntable is moved to the center of the clamp (① in Fig. 27) by adjusting the two micrometers, which are recorded as $X_1 = 1.568$ mm and $Y_1 = 4.852$ mm in the X and Y directions. Then, the torsion fiber (② in Fig. 27) at the top of the clamp is rotated by 180°, which moves the clamp to the position shown by the dashed circle in the figure. The turntable is rotated by one turn again, and its rotation axis is moved to the new location of the clamp's center (③ in Fig. 27) by adjusting the two micrometers. This shifts the readouts of the two micrometers to $X_3 = 1.615$ mm and $Y_3 = 4.965$ mm, respectively. Finally, the rotation axis of the turntable is aligned with the torsion fiber by adjusting the two micrometers to the mean positions of $X_2 = (X_1 + X_3)/2$ and $Y_2 = (Y_1 + Y_3)/2$. The uncertainties of the alignment in the X and Y directions are 9 [7] and 13 [10] μm in experiment I [II], respectively.

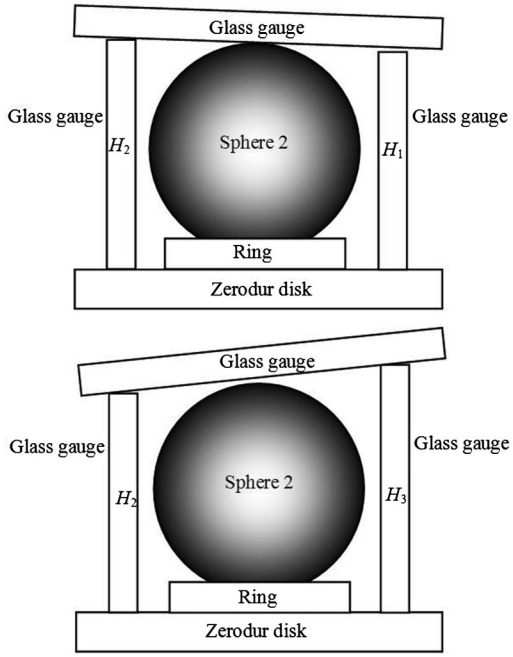

FIG. 26. Schematic diagram for determining the center height of sphere 2 (similarly for sphere 4). The three vertical glass gauges have heights of H_1, H_2, and H_3, respectively, with an incremental height of 10(1) μm. In the upper (lower) drawing, there is no gap (a gap) between the horizontal glass gauge and sphere 2 in the vertical axis.

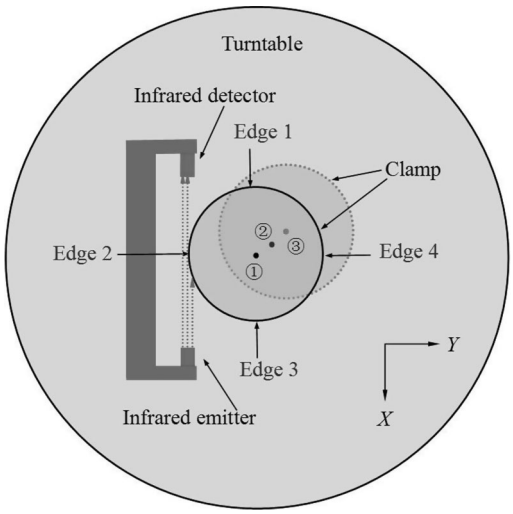

FIG. 27. Schematic diagram for aligning the rotation axis of the turntable to the torsion fiber. The infrared detector fixed on the turntable monitors the deviation between the cylindrical clamp and the rotation axis of the turntable. The rotation axis of the turntable is first moved to the clamp's center ①. Then the torsion fiber located at ② is rotated by 180°, moving the clamp's center to ③. The rotation axis of the turntable is moved to the new location of the clamp's center. By using the coordinates of ① and ③, the rotation axis of the turntable is aligned with the torsion fiber ②.

The deviation between the torsion fiber and the clamp's center is calculated by $\Delta X_{fc} = (X_3 - X_1)/2$ and $\Delta Y_{fc} = (Y_3 - Y_1)/2$, which yield 24(9) [17(7)] and 56(13) [45(10)] μm in the X and Y directions in experiment I [II], respectively. Under the assumption of a flexible fiber, the deviations, calculated from the geometry metrology and mass distribution of the pendulum system, are found to be 18 and 53 μm in the X and Y directions, respectively. These values agree well with the measured deviations within the errors.

The top supporting point of the torsion fiber shifts from air to the vacuum condition due to a deformation of the chamber. The positions of the fiber in air and in vacuum are compared by using the three telescopes. By taking this shift into account, the turntable is adjusted beforehand in air. The measured results of the center deviation between the clamp and turntable in vacuum are 7(9) [14(7)] and 73(13) [68(10)] μm in the X and Y directions in experiment I [II], respectively, as shown in Fig. 28. Finally, the rotation axis of the turntable is aligned with the torsion fiber in vacuum with uncertainties of 19 [7] and 22 [25] μm in the X and Y directions in experiment I [II], respectively.

One of the telescopes is initially used to monitor the change of the Zerodur disk in the Z direction from air to the vacuum condition (just as monitoring the pendulum in the Z direction), and no change is observed because the Zerodur disk and the turntable are fixed tightly to the base of the vacuum chamber. The tilt of the base of the vacuum chamber is monitored by placing the two tiltmeters on the Zerodur disk, and the outputs are compared from air to vacuum. No distinct changed is observed at the level of 1 μrad, which means that the variation of the two source masses in the Z direction is less than 0.1 μm from air to vacuum, much less than the uncertainty of the alignment in the Z direction. Therefore, the two tiltmeters are placed at the base of the vacuum chamber in air in normal running experiments. The function of the tiltmeters is to monitor the sudden disturbances from the seismic noise, which provides one of the criteria to remove the polluted data.

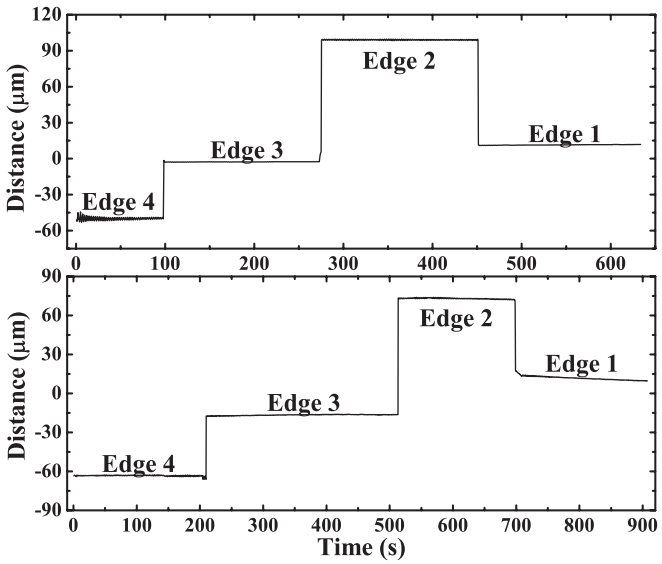

FIG. 28. The observed final center deviations between the clamp and the rotation axis of the turntable in experiment I (upper) and II (lower), respectively. As shown in Fig. 27, the X direction is from edges 1 to 3, and the Y direction is from edges 2 to 4. The observed curves show a larger deviation in the Y direction.

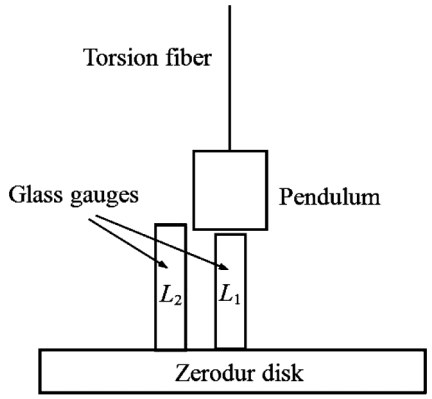

FIG. 29. Schematic diagram for determining the center height of the pendulum (side view). Two glass gauges ($L_2 = L_1 + 10$ μm) are used to measure the separation between the pendulum and the Zerodur disk. By adjusting the height of the pendulum, the shorter glass gauge can be inserted into the separation, but the longer gauge cannot.

6. Center height of the pendulum

The center height of the pendulum is required to coincide with that of the source masses. The vertical position of the pendulum is measured by using two glass gauges with a height difference of 10(1) μm, as shown in Fig. 29. First, the longer glass gauge is inserted under the pendulum body, and the pendulum is lowered slowly by adjusting the vacuum feedthrough until the pendulum is no longer free. Then, the longer glass gauge is removed and the shorter one is inserted. The pendulum is lowered further to touch the shorter gauge and the travel range of the feedthrough is recorded. Finally, the pendulum is raised by half of the travel range, and the feedthrough in the Z direction is locked. One of the three telescopes mentioned in Sec. II E 5 is used to monitor the change in the height of the pendulum body from air to vacuum. After several repeated adjustments and by taking the height of the pendulum body into account, the center height of the pendulum is determined to be 34.250(8) [34.205(12)] mm in experiment I [II]. Compared with the center heights of the source masses measured in Sec. II E 4, the differences in the center heights between the pendulum and the source masses in experiment II is smaller than that in experiment I by a factor of about 3.

7. Attitude of the pendulum

The attitude of the pendulum, represented by angles $\Delta\theta_x$ and $\Delta\theta_y$ about the X and Y axes, respectively, is measured by a commercial ELCOMAT 3000 electronic autocollimator [66]. As shown in Fig. 30, the two opposite end surfaces of the pendulum body are alternately monitored by rotating the pendulum about the torsion fiber by 180°. In each position, the pendulum remains stationary with the help of a very soft cantilever for 6–8 minutes, and the measurement is repeated for more than 6 times. The typical data segments in measuring the two angles in experiments II are shown in Fig. 31.

The parallelism between any two opposite surfaces of the pendulum is better than 5 μrad, which can be neglected in determining the attitude of the pendulum. Upon averaging, the two angles are $\Delta\theta_x = 4.06(5)$ [4.07(2)] mrad and $\Delta\theta_y = -1.91(2)$ [$-1.63(2)$] mrad in experiment I [II], which will be used to correct the calculation of the gravitational coupling coefficient $I/\Delta C_g$.

8. Angle θ_0

We define the angle between the center line of the source masses and the equilibrium azimuthal position of the pendulum as θ_0. We first tried to measure θ_0 by switching the source masses from the near to the far position and recording the change in the equilibrium position of the pendulum. This measurement usually lasted several hours to acquire an accurate equilibrium position. However, because of the thermal effect from rotating the turntable frequently and the drift of the torsion fiber, we did not obtain a satisfactory result.

In practice, θ_0 is measured by an indirect method, called a "*transferring-reference method*." The long glass ruler, used in positioning the spheres in Sec. II E 2 (see Fig. 25), is put on the Zerodur disk leaning against the source masses, as shown in Fig. 32. The center line of the source masses is then transferred onto the surface of the glass ruler. Now, the pendulum is rotated slightly and the fixed ELCOMAT 3000 electronic autocollimator [66] aimed at the glass ruler records this angle θ_g. Then, the pendulum is rotated back to be approximatively in line with the glass ruler, and the free oscillation of the pendulum is recorded by the autocollimator. The resulting angle-time data are used to extract the equilibrium position of the pendulum θ_p. At the same time, the optical lever, which is mounted on the opposite side of the autocollimator and aimed at the mirror on the top of the pendulum body, also monitors the

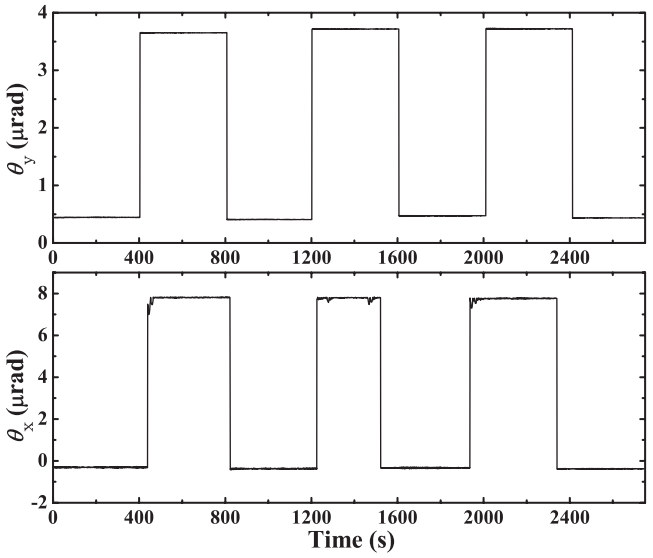

FIG. 31. Typical data segment in measuring attitude angles $\Delta\theta_y$ and $\Delta\theta_x$ in experiment II. Since the suspended pendulum is not upright exactly, the output of the autocollimator jumps to another value when the pendulum is rotated about the torsion fiber by 180°. Half of the change corresponds to the tilt of the pendulum.

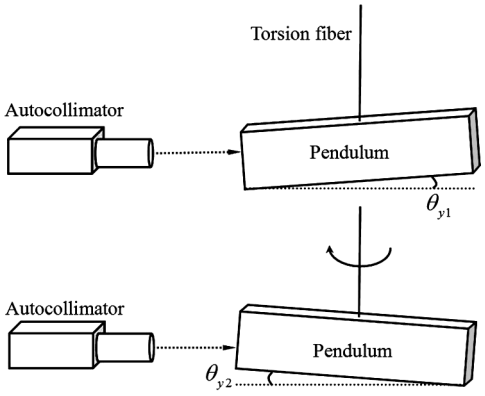

FIG. 30. Schematic drawing for measuring $\Delta\theta_y$. Upper: The Y-axis output of the autocollimator measures θ_{y1}. Lower: The torsion fiber is rotated by 180° and the Y-axis output measures θ_{y2}. We obtain $\Delta\theta_y = (\theta_{y1} - \theta_{y2})/2$.

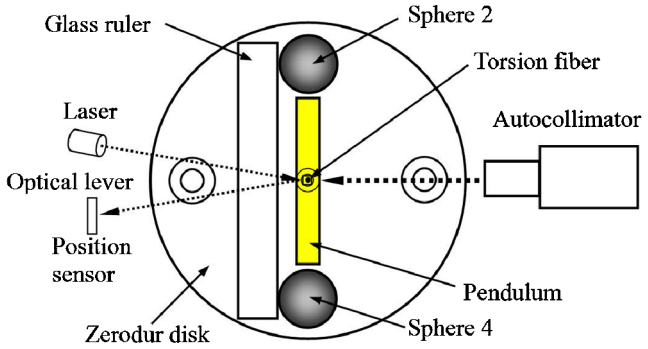

FIG. 32 (color online). Schematic diagram for determining the angle θ_0 with a transferring-reference method. The center line of the source masses is first transferred to the glass ruler and then to the autocollimator, which is further transferred to the position sensor of the optical lever by monitoring the free oscillation of the pendulum synchronously.

free oscillation of the pendulum synchronously. This also determines the equilibrium position of the pendulum. This way, the center line of the source masses is further transferred onto the fixed position sensor of the optical lever. Thereafter, the long glass ruler and the autocollimator are removed, and the angle between the center line of the source masses and the pendulum can be obtained from $\theta_0 = \theta_p - \theta_g$. Finally, the turntable is rotated to be in line with the pendulum, such that $\theta_g = \theta_p$ or $\theta_0 = 0$.

The determined θ_0 is 0(91) [0(23)] μrad in experiment I [II]. Because of the slow drift of the torsion fiber, the equilibrium position of the pendulum varies slowly. This can be corrected from the angle-time data of the oscillating pendulum when switching the source masses positions from near to far, or whereas.

9. Electrostatic shield

After the above measurements are finished, a 0.7-mm-thick, 94-mm inner diameter, 90-mm-high, hollow gold-coated aluminum cylinder is inserted between the pendulum and the source masses (as shown in Fig. 3). This serves as an electrostatic shield but also appears to improve the

TABLE IV. The error budget of $\Delta C_g/I$ contributed by the errors in the geometrical metrology and mass distributions of the pendulum and source masses. The dimensions are all converted to the corresponding values at 20.20 °C. The values in the square brackets are for experiment II.

Parameter	Measured value	Uncertainty	$\delta G/G$ (ppm)
Torsion pendulum:			
Mass	63.383 88 g	0.000 21 g	0.005
Length	91.465 46 mm	0.000 13 mm	1.86
Width	12.014 71 mm	0.000 05 mm	0.54
Height	26.216 18 mm	0.000 07 mm	0.22
Tilt $\Delta\theta_x$	4.06 [4.07] mrad	0.05 [0.02] mrad	0.11 [0.04]
Tilt $\Delta\theta_y$	−1.91 [−1.63] mrad	0.02 mrad	0.07 [0.06]
Density inhomogeneity $\Delta\rho/\rho$	0	0.92×10^{-5}	<0.21
Chamfer properties	0	$<45''$	0.34
Coating layer:			
Mass	49.863 mg	0.026 mg	0.01
Ratio of layer thickness:			
Side face: end face	0.824	0.041	4.30
Bottom face: end face	0.782	0.023	0.36
Top face: end face y_0	0.51	0.01	0.15
Top face: end face A	−0.286	0.024	0.09
Top face: end face t	13.3 mm	2.4 mm	0.27
Clamp:			1.62
Ferrule:			0.30
Mirror:			0.03
Glues:			0.10
Chips:			0.18
Source masses:			
Mass of sphere 2	778.1794 [778.1796] g	0.0009 g	0.58
Mass of sphere 4	778.1763 [778.1756] g	0.0009 g	0.58
Density inhomogeneity	0	7.56×10^{-3}	4.50
Distance of GCs	157.161 54 [157.370 11] mm	0.000 37 mm	9.64 [9.61]
Relative positions:			
Centric height of pendulum	34.250 [34.205] mm	0.008 [0.012] mm	0.76 [0.40]
Centric height of sphere 2	34.176 [34.229] mm	0.006 [0.007] mm	0.09 [0.11]
Centric height of sphere 4	34.188 [34.218] mm	0.006 mm	0.47 [0.25]
Position of fiber in X axis	0	0.013 [0.007] mm	0.44 [0.15]
Position of fiber in Y axis	0	0.013 [0.025] mm	0.45 [1.21]
Position of turntable in X axis	0	2 μm	0.02
Position of turntable in Y axis	0	2 μm	0.05
θ_0	0	91 [23] μrad	0.06 [0.01]
90° accuracy of turntable	0	145 μrad	0.001
Total:			
$\Delta C_g/I$ in experiment I	25 202.85 kg · m^{-3}	0.30 kg · m^{-3}	11.85
$\Delta C_g/I$ in experiment II	25 066.58 kg · m^{-3}	0.30 kg · m^{-3}	11.85

stability of the pendulum's period. To minimize the electrostatic coupling between the shield and the pendulum, the potential difference between them needs to be nulled. The procedure of nulling this potential difference will be discussed in Sec. IV E.

F. Determination of $\Delta C_g/I$

With the geometrical metrology and mass distributions of the pendulum and source masses determined, the gravitational coupling coefficient $\Delta C_g/I$ in Eq. (7) now can be calculated. The detailed algorithm is given in Appendix B. The magnitude of $\Delta C_g/I$ is found to be 25 202.85(30) [25 066.58(30)] $\mathrm{kg}\cdot\mathrm{m}^{-3}$ in experiment I [II], which contributes an uncertainty of $u_r = 11.85$ ppm to the G value in both experiments. The 209-μm difference in the center distances of the source masses mainly accounts for the difference in $\Delta C_g/I$ between experiments I and II.

The error budget of $\Delta C_g/I$ in determining G is listed in Table IV. The largest uncertainty is from the center distance of the two spheres, which contributes $u_r = 9.64$ [9.61] ppm to the G value in experiment I [II]. The main limitation comes from the nonsphericity of the two spheres. The major uncertainty from the pendulum comes from the coating layer, which brings a correction of -24.28 ppm to the G value with an error of 4.33 ppm. The dimensions of the pendulum provides an error of 1.95 ppm, which is mainly from the uncertainty in measuring its length.

III. DATA ACQUISITION

A personal computer (PC) containing a PCI-6014 interface card [67] is used to record the pendulum twist continuously, and another PC of the same type monitors three important environmental parameters: the temperature, seismic disturbances, and fluctuations of the air pressure. The 16-bit card has eight pairs of analog input channels of analog-to-digital converter and two output channels of digital-to-analog converter (DAC). One of the DAC channels is used to provide a compensating voltage to the electrostatic shield cylinder, as will be discussed in Sec. IV E.

All the data are taken at a regular interval of 0.5 s at the two PCs triggered by a quartz crystal oscillator [68]. The oscillator is calibrated by a SR620 Universal Time Interval Counter [69] and is found to have a frequency accuracy and stability of $\pm 5 \times 10^{-9}$ Hz and 2×10^{-10}/day, respectively.

A. Optical lever

The pendulum rotation angle is monitored by an optical lever, as shown in Fig. 33. The light beam from a He-Ne laser ($P = 0.6$ mW, $\lambda = 632$ nm) is square-wave modulated at 812 Hz by the SR540 chopper [70] and then

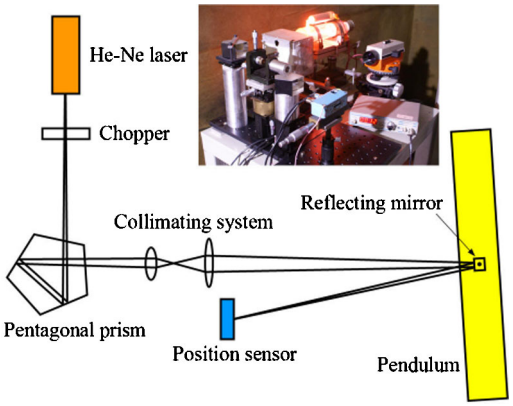

FIG. 33 (color online). Schematic diagram (top view) and photograph of the optical lever used to monitor the pendulum twist.

reflected by a pentagonal prism. After passing through a circular collimator, the light forms a 1-mm-diameter parallel beam, directs onto the reflecting mirror that is attached on the top of the pendulum, and finally focuses onto the linear positioning sensor [71], located about 500 mm from the pendulum.

The currents from the two ends of the position sensor (L and R signals) are first converted to the voltage signals in a low-noise electronic circuit and go through two SR830 lock-in amplifiers [72]. Then, L and R signals are digitized in the analog-to-digital converter and are summed to get $\Sigma = L + R$ and subtracted to get $\Delta = L - R$, which are stored into the hard disk of the PC. The pendulum twist is extracted from the ratio Δ/Σ, which reduces the effect of the laser's power variation. The angle-time data of the pendulum are recorded continuously by the PC at the regular sampling rate of 2 Hz.

The pendulum rotation angle θ is obtained from $\theta = \alpha(\Delta/\Sigma)$, and the coefficient α is calibrated by using the ELCOMAT 3000 electronic autocollimator [66]. The autocollimator is not used to directly monitor the pendulum twist because its output is a discrete series. By using the synchronous data recorded by the optical lever and the autocollimator, α is fitted by the least-square method and yields $\alpha = 11.360(86)$ [11.478(3)] mrad/(Δ/Σ) in experiments I [II], as shown in Fig. 34.

B. Environmental monitors

Three types of environmental signals are monitored continuously during the experiment. Six temperature sensors (four inside the vacuum chamber) are used to monitor the environmental temperature variations. All the sensors are calibrated together with the CST6502 standard digital thermometer [73], and the output differences among them are less than 0.001 °C. Two tiltmeters mounted on the vacuum chamber support frame in two orthogonal directions monitor the seismic disturbances during the experiment. One barometer monitors the fluctuation of the air

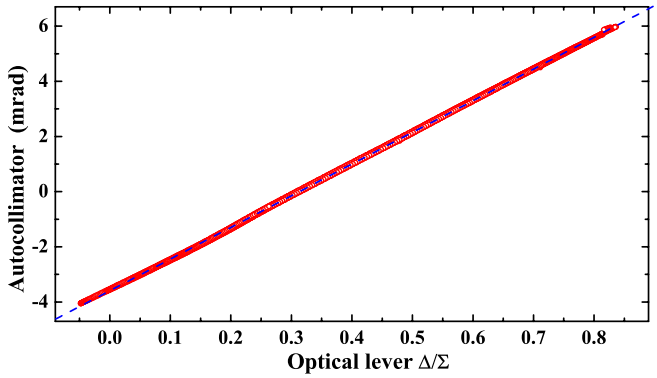

FIG. 34 (color online). Calibrating the coefficient α in $\theta = \alpha(\Delta/\Sigma)$ by the pendulum twist synchronously recorded by the optical lever and the ELCOMAT 3000 electronic autocollimator in experiment II. The data are accumulated over in five full oscillations. The outputs from the autocollimator and the optical lever are set as Y and X, respectively, and the linear fit (dashed line) of the two outputs yields $\alpha = 11.478(3)$ mrad$/(\Delta/\Sigma)$.

pressure. All these quantities are recorded for off-line analysis.

The data acquisition system, lock-in amplifiers, and other related instruments are all located in a room 10 m away from the room of the vacuum chamber, which is thermally isolated to further reduce the effects of the environmental temperature variation.

IV. SYSTEMATIC EFFECTS

A. Strategy

In our G measurements, the systematic effects are studied by identifying possible error sources (temperature variations, oscillation amplitude of the pendulum, electrostatic and magnetic fields, etc.) and making individual measurements in which, one at a time, each of these error-causing variables is deliberately magnified to cause a perceptible change in the pendulum's period. The ratio of the induced change in the period to the magnitude of the variable is taken as the sensitivity to the corresponding variable. The systematic effects are determined by multiplying these sensitivities with the measured changes of the error-causing variables during our experiments.

B. Properties of torsion fiber

1. Thermal noise

The thermal noise of the pendulum [53] is a fundamental limit in determining the pendulum's period in the time-of-swing method [74–79]. The error in the period can be written as [34,80]

$$\delta T \approx \frac{T}{A_0}\sqrt{\frac{K_b \mathcal{T}}{K\omega Q \tau_m}}, \tag{21}$$

where T and A_0 are the oscillation period and initial amplitude of the pendulum, respectively, $\omega = 2\pi/T$, K and Q represent the torsion spring constant and the quality factor of the fiber, respectively, and K_b, $\mathcal{T}$, and τ_m are the Boltzmann constant, ambient temperature, and time duration of the data, respectively.

In our G experiments, the typical duration of τ_m is three days for one data segment taken at the near or far position. According to Eq. (21), δT is about 0.08 ms and contributes an uncertainty of $u_r \approx 30$ ppm to the G value, if only one set of data is used. If the measurements from the near to far positions are repeated n times, this error decreases to $u_r = 30/\sqrt{n}$ ppm, equivalent to an increase in the integration time by $n\tau_m$.

2. Thermoelastic effect

The torsion spring constant is an intrinsic property of the torsion fiber, which can be expressed as

$$K = \frac{\pi D^4 S}{2l}, \tag{22}$$

where l and D are the length and diameter of the torsion fiber, respectively, $S = E/2(1+\mu)$ is the shear modulus, and E and μ are the Young's modulus and Poisson ratio of the fiber, respectively. Because the parameters l, D, and E are the linear functions of the temperature in a limited range [81], the spring constant of the fiber is temperature-dependent, thus named the thermoelastic effect. For a small temperature change $\Delta\mathcal{T} = \mathcal{T} - \mathcal{T}_r$, the torsion spring constant can be expressed as [82,83]

$$K = K_0(1 + \alpha_K \Delta\mathcal{T}), \tag{23}$$

where α_K is the temperature coefficient of K, and K_0 is the torsion spring constant at the reference temperature $\mathcal{T}_r$. For a torsion pendulum, the period is expressed as $T = 2\pi\sqrt{I/K}$, and hence the coefficient α_K can be decomposed into two parts:

$$\alpha_K = \alpha_I - 2\alpha_T. \tag{24}$$

Here α_I is the temperature coefficient of the moment of inertia of the pendulum, which can be calculated from the thermal expansion of the pendulum, and α_T represents the temperature coefficient of the pendulum's period, defined by

$$\alpha_T = \frac{\Delta T}{T}\frac{1}{\Delta\mathcal{T}}, \tag{25}$$

where ΔT is the change in the period T due to the change in the temperature $\Delta\mathcal{T}$. Therefore, we can measure $\Delta T/\Delta\mathcal{T}$ and determine α_T and hence α_K.

We investigate the thermoelastic property of the fiber used by means of the method described in Ref. [82]. A quartz disk pendulum is designed to have a mass of 62.913 (1) g and a moment of inertia of $3.5304(15) \times 10^{-5}$ kg m^2. The disk pendulum has two major merits: (i) it eliminates the coupling to the background gravitational gradient, and

(ii) the pendulum is made from the quartz glass so that its moment of inertia is insensitive to the temperature change due to the lower thermal expansion coefficient. The resulting α_I is $1.19(1) \times 10^{-6}/°\mathrm{C}$, a factor of 40 smaller than that of the aluminum disk pendulum used in Ref. [82].

The temperature of the environment is modulated by six 60-W bulbs, which are covered with six iron barrels and located at the corners of our cave laboratory. The changes in the temperature near the pendulum and the torsion fiber in vacuum are monitored by the temperature sensors with a resolution of 0.0005 °C. The pendulum twist is monitored by the optical lever synchronically. In each cycle of temperature modulation, the change of the temperature exceeds 0.5 °C. The periods are extracted from the angle-time data by a correlation method for 20 full oscillations [80,84–86]. A typical modulation of the environmental temperature and the corresponding period change are shown in Fig. 35.

Figure 36 shows a typical period of the pendulum versus the ambient temperature. The circles are the experimental values of the period T at different temperature $\mathcal{T}$, and the solid line represents the linear-fitting result of T varying with $\mathcal{T}$. The slope of the fitted line is 32.4(2) ms/°C, which indicates the rate of the change in the period with the temperature, and the resultant α_T is $72.3(5) \times 10^{-6}/°\mathrm{C}$. From Eq. (24), α_K is calculated to be $-144.6(1.4) \times 10^{-6}/°\mathrm{C}$. Combined with two other repeated measurements which yield α_K of $-143.2(1.4) \times 10^{-6}/°\mathrm{C}$ and $-147.2(1.4) \times 10^{-6}/°\mathrm{C}$, the mean value of α_K is determined to be $-145(2) \times 10^{-6}/°\mathrm{C}$.

The variation in the period of the pendulum subject to the thermoelastic effect during the experiment is corrected in determining $\Delta\omega^2$. The corrections for the G value resulting from the fluctuations of the environmental temperature amount to $-39.83(1.52)$ [8.37(0.82)] ppm in experiment I [II], in which the reference temperature $\mathcal{T}_r$ is set to be 20.20 °C. In experiment II, $\mathcal{T}$ is more close to $\mathcal{T}_r$; therefore, a smaller correction is introduced.

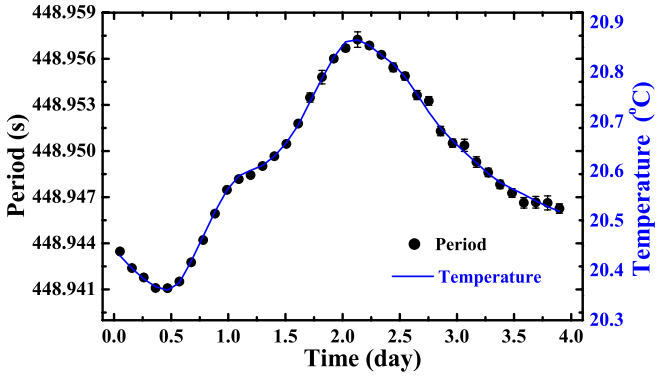

FIG. 35 (color online). Typical variations of the pendulum's period and temperature with time. Each solid circle denotes the pendulum's period in 20 full oscillations, extracted by the correlation method. The error bars in some circles are smaller than the size of the circle. The line represents the modulated temperature.

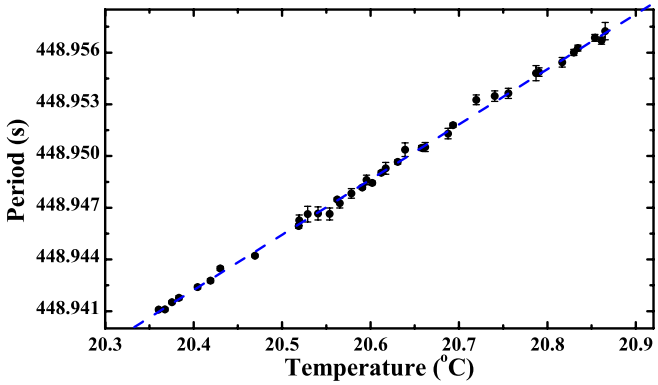

FIG. 36 (color online). The period of the pendulum versus the environmental temperature. The solid circles represent the period T at different temperature $\mathcal{T}$ (extracted from Fig. 35), and the error bars in some circles are smaller than the size of the circle. The dashed line represents the least-square fit.

3. Nonlinear effect

In the linear approximation, the angular frequency ω of a torsion pendulum is independent of its amplitude. If we consider the nonlinear properties in which the period of the pendulum oscillation varies with its amplitude, the typical equation of the oscillation should be written as [82,87,88]

$$I\ddot{\theta} + \gamma\dot{\theta} + K\theta + K_3\theta^3 = 0, \tag{26}$$

where γ is the damping coefficient and K_3 is the nonlinear coefficient of the pendulum. In the G measurement with the time-of-swing method, K_3 consists of three parts: K_{3f}, K_{3g}, and K_{3b}, which represent the nonlinear effects of the fiber, source masses, and background gravitational field, respectively. The approximate solution of Eq. (26) at a small amplitude can be expressed as [82,89,90]

$$\theta(t) \approx A_0 e^{-\beta t}\cos\omega t + \frac{K_3}{32K}A_0^3 e^{-3\beta t}\cos 3\omega t, \tag{27}$$

where A_0 is the initial amplitude of the oscillating pendulum and $\beta = \gamma/2I$, with I denoting the moment of inertia of the pendulum. The period of the pendulum varies with its amplitude A and can be written as

$$T(A) = T_0\left(1 + \frac{\beta^2}{2\omega_0^2} - \frac{3K_3}{8K}A^2\right), \tag{28}$$

where $\omega_0^2 = K/I$, and $T_0 = 2\pi\sqrt{I/K}$ is the unperturbed period of the pendulum. From Eqs. (7) and (28), the uncertainty in the G value contributed by the nonlinear effect can be estimated by

$$\frac{\delta G}{G} = \frac{3A(A\Delta K_3 + 2K_3\Delta A)}{4I\Delta(\omega_0^2)}. \tag{29}$$

The nonlinear property of the used fiber is studied by means of the method described in Refs. [89,90], and the same experimental setup as that in studying the thermoelastic property (described in the above section) is used. Because of the absence of the source masses, $K_{3g} \approx 0$, and K_{3b} is also neglectable because the disk pendulum is insensitive to the background gravitational gradient. Therefore, only K_{3f} remains.

The pendulum is excited to oscillate with an initial amplitude of ~11 mrad, and it gradually attenuates to ~2.2 mrad in four days due to dissipation in the fiber. Then, the feedthrough is adjusted to reset the pendulum to almost the same initial amplitude for the next set of the experiment. The pendulum's period and amplitude varying with time in three consecutive data sets are shown in Fig. 37. Each circle and triangle represent the average period and amplitude of the pendulum, respectively, over 20 full oscillations. The thermoelastic property of the fiber has been corrected by using the measured coefficient given in Sec. IV B 2.

The result shows that the change of the period with time is not due to the nonlinearity of the fiber, because the period does not change abruptly when the amplitude is reset. It appears that the variation of the period is due to aging of the fiber. Because the pendulum is running in a high vacuum with Q of ~1700, the damping term in Eq. (28) is $\beta_0^2/2\omega_0^2 = 1/8Q_o^2 \approx 4.3 \times 10^{-8}$ and is negligible. In order to model the aging effect of the fiber, we introduce two parameters: a linear coefficient η_W and an exponential attenuation coefficient b_W. We fit the period and amplitude by using

$$T(A) \approx T_0\left(1 - \frac{3K_{3f}}{8K}A^2\right) + \delta T_0(1 - e^{-b_W t}) + \eta_W t. \tag{30}$$

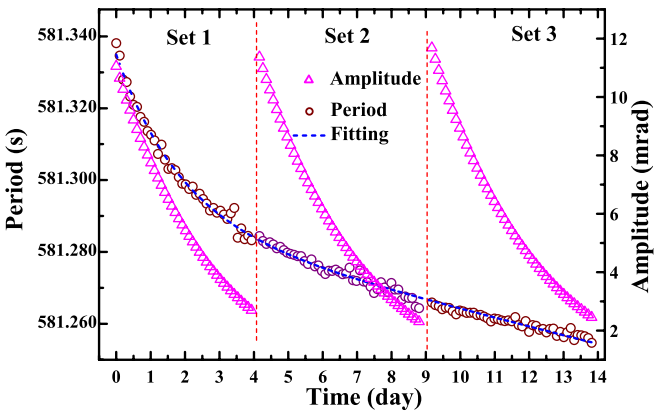

FIG. 37 (color online). The period and amplitude of the disk pendulum versus time in three consecutive sets of experiments. Each circle and triangle represent the average period and amplitude of the pendulum over 20 full oscillations, respectively. The three sets have almost the same initial amplitudes. The dashed line shows a fit for the period according to Eq. (30).

This yields $K_{3f}/K = -4.3(9.2) \times 10^{-3}$ rad^{-2}, $\eta_W = 1.77(6)$ ms/day, and $b_W = 0.52(2)$ ms/day, respectively.

Since the measured data yield a null result for the nonlinear effect of the torsion fiber within the error, we take the maximum value to estimate its effect in the G measurement. By choosing $K_{3f}/K = -13.5 \times 10^{-3}$ rad^{-2} and other typical parameters in our G measurements, we find the uncertainty due to the nonlinearity of the fiber to be less than 0.7 ppm.

4. Aging effect

The aging of the fiber has a great effect on the pendulum's period, which consists of two parts, as discussed in Sec. IV B 3. One is the exponential attenuation, which mainly appears at the beginning of each reloading of the pendulum. The other is the linear term, which decreases uniformly at the rate of about $\eta_W \sim -0.5$ ms/day at both the near and far positions in the duration of about 66 [42] days in experiment I [II] (as shown in Figs. 42 and 43 in Sec. V D). To overcome the aging effect, the so-called $A - B - A$ method is used to obtain $\Delta(\omega^2)$ from the near and far positions. In this case, the aging effect of the fiber introduces only $u_r < 0.01$ ppm to the G value.

5. Anelastic effect

The frequency dependence of the fiber's spring constant [38], named the anelastic effect, also introduces a systematic error in the measurement of G with the time-of-swing method. Following Eq. (7), this correction can be expressed as

$$\frac{\Delta G}{G} = \frac{\Delta K}{I\Delta(\omega^2)}. \tag{31}$$

We first studied the frequency dependence of the fiber used by employing two disk pendulums with different moments of inertia (for a detail description, see Ref. [91]). The ratio of the moments of inertia of the two pendulums is determined precisely by a quartz fiber with $Q \approx 3.36 \times 10^5$, whose anelastic effect is negligible. The experimental result indicates that the torsion spring constant of the tungsten fiber used in our G measurements is dependent on the oscillation frequency by $\Delta K/\Delta(\omega^2) = (0.954 \pm 0.084) \times 10^{-8}$ kg m^2 at ~mHz range. This contributes a bias in our G measurements up to $\Delta G/G = (211.80 \pm 18.69)$ ppm. The main uncertainty is due to the fluctuations of the pendulum period caused by the frequent reloading of the tungsten fiber. Exchanging the pendulums every 5 or 15 days resulted in a larger exponential aging effect at the beginning of each data set and affected the stability and repeatability of the pendulum's period.

In our G measurements, the Q of the main torsional fiber is ~1700. The observed result due to the fiber's anelasticity is slightly larger than the upward fractional bias of $1/\pi Q$

predicted by Kuroda [38] but smaller than the upper bound of $1/2Q$ proposed by Newman and Bantel [34,92].

C. Gravitational nonlinearity of source masses

As mentioned in Sec. IV B 3, because of the finite amplitude of the pendulum's oscillation, the nonlinear component K_{3g} of the gravitational field due to the source masses shifts the pendulum's angular frequency squared from ω_0^2 to

$$\omega^2 = \omega_0^2\left(1 + \frac{3K_{3g}}{4K}A^2 + \frac{3K_{3g}}{K}\theta_0^2\right). \tag{32}$$

The term associated with the angle θ_0 rises from the misalignment between the equilibrium position of the pendulum and the center line of the source masses. The nonlinear coefficient K_{3g} can be calculated by a numerical integration, and it is related to the gravitational potential V_g between the pendulum and the source masses by

$$K_{3g} = \frac{1}{6}\frac{\partial^4 V_g(\theta)}{\partial\theta^4}, \tag{33}$$

where θ is the angle between the pendulum and the center line of the source masses. By substituting the typical values of the pendulum and the source masses and their positions into Eq. (33), K_{3g} is computed at the near and far positions, as listed in Table V.

The gravitational nonlinearity of the source masses is corrected in determining $\Delta\omega^2$, and the resultant corrections to the G values are 7.73(0.30) and 4.79(0.20) ppm in experiment I and II, respectively. The quantity difference is mainly due to the differences in the center distances of the spheres (Sec. II E 3), angle θ_0 (Sec. II E 8), and amplitudes of the pendulum in the experiments.

D. Magnetic effect

The time-varying magnetic field in the environment can lead to a systematic error in the pendulum's period because the pendulum has a weak magnetic moment. We first measure the time-varying component of the ambient magnetic field at the location of the pendulum and then increase the local magnetic field by using two coils to observe the response of the pendulum [93]. The change of the pendulum's period observed is used to estimate the effect from the local magnetic fields to our G value.

A three-axis flux-gate magnetometer [65] is placed at the usual location of the pendulum in the vacuum chamber, and the magnetic field is recorded continuously for over 200 hours. The observed geomagnetic field in the X direction and its spectral density are shown in Fig. 38. The amplitude at the pendulum's frequency 1ω is only 1.7×10^{-5} G in the X direction. We obtain similar amplitudes in the Y and Z directions of $\sim 1.4 \times 10^{-5}$ G. Therefore, the amplitude of the time-varying magnetic field vector at 1ω is $< 3 \times 10^{-5}$ G. Because of the shielding by the mu-metal and vacuum chamber itself, the observed amplitudes are several times smaller than those of the geomagnetic field outside of the laboratory.

To observe the variation in the period induced by the external magnetic field, a square-wave magnetic field is applied at the location of the pendulum by using the coils, which are placed outside the vacuum chamber in the X and Y directions, about 250 mm from the pendulum. The currents in the coils are reversed every eight hours and the three components of the magnetic field are recorded. The changes in the X and Y directions are found to be 2.991(4) and 3.144(4) G, respectively. The change in the Z direction is 1 order of magnitude smaller and can be neglected. Then, the pendulum is subjected to the same external magnetic field and its response is monitored by the optical lever.

The changes in the pendulum's period induced by the magnetic field in the Y and X directions are shown in Fig. 39. For each 8-hour data segment, the average period is extracted from the angle-time data. After removing the aging effect, the average changes in the periods are determined to be 115(2) and 27(2) ms corresponding to the magnetic fields of 3.144(4) G in the Y direction and 2.991(4) G in the X direction, respectively. The magnetic field sensitivity of the period is 37(1) ms/G in the Y

TABLE V. Gravitational nonlinear components of K_{3gn} and K_{3gf} in experiments I and II. Units: 10^{-10} N m rad^{-3}

Parameters	K_{3gn} (near)	K_{3gf} (far)
Experiment I	−1.6017	−0.0075
Experiment II	−1.5865	−0.0073

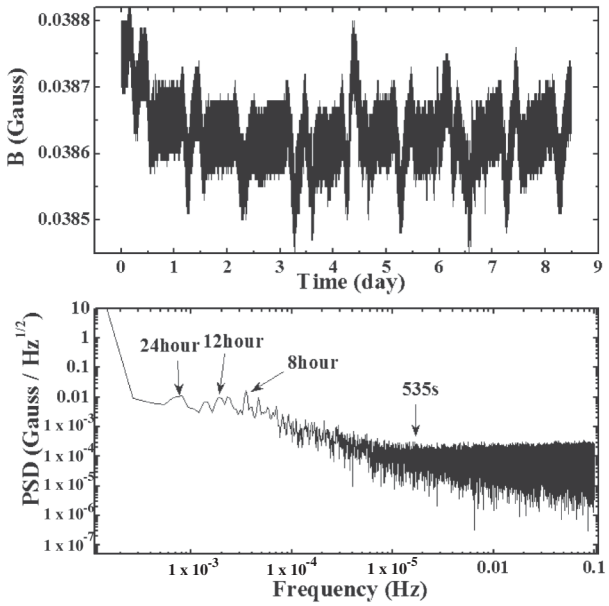

FIG. 38. The X component of the magnetic field (upper) at the location of the pendulum and its spectral density (lower).

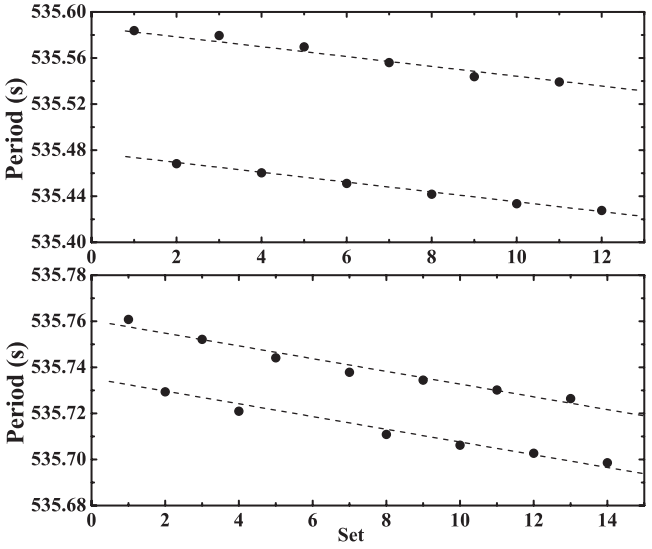

FIG. 39. The changes in the period induced by magnetic field in the Y (upper) and X (lower) directions. The linear drifts (dashed line) apparent in the two graphs are attributed to the aging effect and are corrected for in data analysis.

direction and 12(1) ms/G in the X direction. Apparently, the period is affected more by the Y component of the magnetic field because a larger surface of the pendulum faces the Y direction.

Next, sinusoidal magnetic fields with an amplitude of about 5×10^{-4} G and periods of 532.4 and 535.8 s are applied in the Y direction when the pendulum is at the near and far positions, respectively. The period of the modulated magnetic field is slightly smaller (larger) than that of the pendulum at the near ("far") position. The magnetic field sensitivity of the pendulum's period is found to be consistent with that of square-wave modulation, but the sign is changed from positive to negative because the periods of modulated magnetic fields are not equal to that of the pendulum exactly.

To calculate the upper limit of the period's change due to time-varying magnetic field of the ambient environment, the Y-direction sensitivity of 37(1) ms/G is chosen. We find $\Delta T < 1.1 \times 10^{-6}$ s, which corresponds an uncertainty of $u_r = 1.1 \times 10^{-6}/3.2 = 0.4$ ppm to the G value, where 3.2 s is the difference of the pendulum's periods at the near and far positions in our G measurement.

E. Electrostatic effect

A perfect electrostatic shield would eliminate the electrostatic interactions between the pendulum and the source masses entirely. However, the practical shield differs from the ideal one, and a slightly different electrostatic potential between the shield and the pendulum body introduces an equivalent electrostatic spring constant K_e [94], which changes the effective K of the torsion fiber. Denoting the potential difference between the pendulum and the shield by ΔU, the electrostatic potential energy W_e can be expressed as

$$W_e = \tfrac{1}{2}C(\Delta U)^2, \tag{34}$$

where C is the capacitance between the pendulum and the shielding cylinder. The electrostatic spring constant K_e can be obtained from

$$K_e = \frac{\partial^2 W_e}{\partial \theta^2} = \frac{1}{2}\frac{\partial^2 C}{\partial \theta^2}(\Delta U)^2. \tag{35}$$

Ideally, the hollow cylinder with perfect radial symmetry would maintain the same potential energy as the pendulum is turned to different orientations, in which $\partial^2 C/\partial\theta^2 = 0$. In reality, however the 0.7-mm-thick cylinder is hard to manufacture precisely, and the pendulum's period changes as

$$\omega^2 = \frac{K_g + K_e}{I} = \frac{K_g}{I} + \frac{1}{2I}\frac{\partial^2 C}{\partial \theta^2}(\Delta U)^2. \tag{36}$$

To find the magnitude of ΔU, a series of voltages are applied to the shield and the response of the pendulum's period is observed. The voltages are varied from -2 to 2 V with an incremental step of 0.5 V over a duration of 1 hour. The angle-time data of the pendulum and the change in the period as a function of the applied voltage are shown in Fig. 40. Following Eq. (36), a quadratic polynomial is used to fit the periods versus the applied voltages, which yields

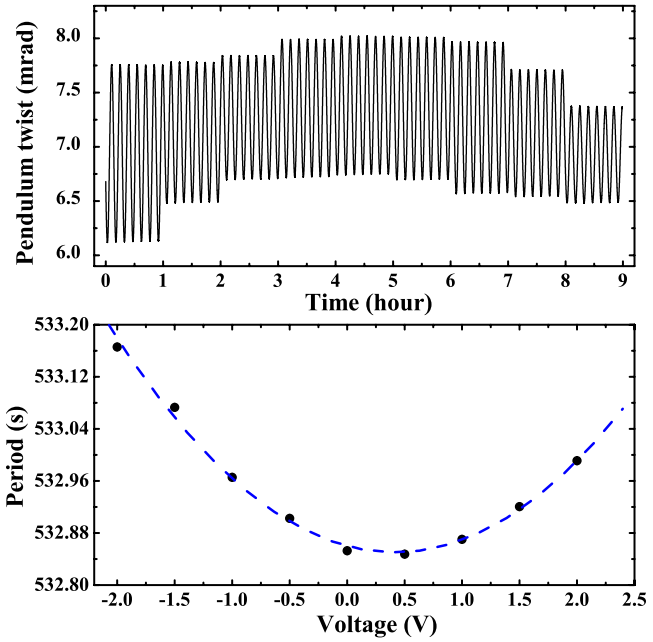

FIG. 40 (color online). Upper: The angle-time data of the pendulum subject to the incremental voltage applied on the shielding cylinder from -2 to 2 V with a step of 0.5 V. Lower: The period as a function of the applied voltage. Each point represents the average period in 1-hour oscillation, and the error is smaller than the size of the circle. The dashed line is the least-square fit with a quadratic polynomial.

$$T = 532.860(1) + 0.056(1) \times [U - 0.420(1)]^2 \text{ s}. \quad (37)$$

This shows that $U = 0.420(1)$ V is the residual potential difference between the shield and the pendulum. This potential is added to the shielding cylinder during the course of our G measurement through one of the 16-bit DAC channels of the interface card [67]. The fluctuation of the applied voltage is less than 1 mV, which brings in an uncertainty of 5.6×10^{-8} s to the pendulum's period and introduces $u_r < 0.1$ ppm to our G value.

The effect due to the patch field [95,96], which refers to the spatial and temporal variations in surface potential of the gold-coated pendulum and the shielding cylinder, also influences the period of the pendulum. This effect cannot be completely canceled by the applied dc voltage because it varies spatially and temporally during the experiment. Accompanying other external random disturbances, the patch field leads the pendulum's period to fluctuate continuously and jointly introduces a larger uncertainty in the period of the pendulum than that predicted by the thermal noise limit, as will be discussed in Sec. V C.

V. ANGLE-TIME SIGNAL MEASUREMENT

A. Data-taking protocols

A standard procedure is used for data taking alternately in the near and far positions. The duration of each data set at one position is about three days, and one typical angle-time data set is shown in Fig. 41. The position is switched by rotating the turntable by approximately $\pm 90°$, taking into account the corrections from the reversal interval of the turntable (Sec. II E 1) and the linear drift of the torsion fiber (Sec. II E 8). An initial amplitude of the pendulum of 2.5–3.0 mrad is achieved by rotating the turntable and using gravitational interaction with the source masses. In the case of measuring the background gravitational effects with the source masses removed, the initial amplitude of the pendulum is adjusted by applying a voltage of about 2 V to the shielding cylinder because of the tiny misalignment between the pendulum and the shielding cylinder. In addition, all the environmental signals are recorded with a sampling time of 0.5 s for off-line analysis.

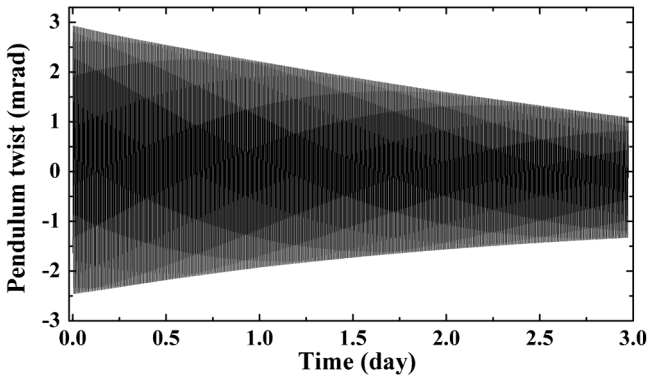

FIG. 41. One 3-day angle-time data segment at the far position from May 20 to May 23, 2007, in experiment I.

From March 21 to May 23, 2007, ten sets of data with the source masses at the near and far positions alternately were taken in experiment I. In addition, the background gravitational effects, including the contributions from the density inhomogeneity of the Zerodur disk, turntable, and misaligned supporting rings, were measured without the source masses, and four sets of background data were accumulated from April 19 to May 12, 2008. No more background data were recorded in experiment I due to the Wenchuan earthquake that occurred at May 12 at Sichuan province in China.

To test the density inhomogeneity of the source masses directly, the positions and orientations of the source masses relative to the pendulum were changed and the G measurement was repeated in experiment II. First, six sets of background data were accumulated from August 25 to September 30, 2008, and then seven sets of experimental data with the source masses at the near and far positions alternately were taken from October 8 to November 19, 2008. After that, the pendulum was removed, and the surface separation between the source masses was remeasured.

B. Correlation method

The oscillation period of the pendulum is extracted from the angle-time data by a correlation method, which has been improved gradually by our group in the past several years [80,84–86]. Compared to the nonlinear least-square fitting method, the correlation method is insensitive to the higher order harmonic oscillations, linear drift, and damping of the pendulum and gives an approximate minimum variance unbiased estimator of the pendulum's oscillation frequency. The basic idea of the correlation method is briefly described below.

In general, a series of the angle-time data $\{y_i\}$ can be expressed as [86]

$$y_i = a\cos(\omega t_i) + b\sin(\omega t_i) + \varepsilon_i, \quad (38)$$

where $\tan^{-1}(b/a) = \phi_0$ denotes the initial phase of the data, $\omega = 2\pi/T$ is the angular frequency of the pendulum, t_i is the sequence of sampling time, and ε_i is a random noise. A standard cosine function $y_t = \cos(\omega_r t)$ with period $T_r = 2\pi/\omega_r \approx T$ is chosen as a reference signal for evaluating the difference in phase ϕ_j $(j = 0, 1, \ldots, m-1)$ with respect to $\{y_i\}$ at the jth period, where m is the number of periods. For each period, the phase angle ϕ_j is determined by the cross-correlation function of the reference signal y_t and the sample data $\{y_i\}$ and can be expressed as

$$\phi_j = \tan^{-1}\frac{b_j}{a_j} = \tan^{-1}\frac{\int_{(j-1)T_r}^{jT_r} y_i(t)\sin(\omega_r t)dt}{\int_{(j-1)T_r}^{jT_r} y_i(t)\cos(\omega_r t)dt}. \quad (39)$$

In numerical calculation, the integral operation in Eq. (39)

is replaced by a summation of the discrete data. The frequency of the reference signal ω_r is close to that of the angle-time data, which is easily obtained by performing a fast Fourier transform analysis.

By substituting Eq. (38) into Eq. (39), choosing the initial phase $\phi_0 \ll 1$ (or $|b| \ll |a|$), and taking the condition $|\varepsilon_i| \ll \sqrt{a^2 + b^2} = A$ into account, ϕ_j can be further expressed as

$$\phi_j = \phi_0 + 2\pi \frac{\omega_r - \omega}{\omega_r} j + \Delta\phi_j, \tag{40}$$

where $\Delta\phi_j$ is a random variable depending on the noise ε_i. From Eq. (39), the mean-square deviation of $\Delta\phi_j$ can be shown to be

$$\langle (\Delta\phi_j)^2 \rangle = \frac{2\sigma^2}{nA^2}, \tag{41}$$

where σ is the standard deviation of the random noise ε_i and n is the number of data points in one full oscillation. By performing a linear fit of Eq. (40), the oscillating frequency ω of the pendulum can be estimated as

$$\tilde{\omega} = \omega_r + \kappa \frac{\omega_r}{2\pi}, \tag{42}$$

where κ is the slope of the fit. The root-mean-square deviation of the unbiased estimator $\tilde{\omega}$ is [86]

$$\sigma_{\tilde{\omega}} = \sqrt{\left\langle \left(\frac{2\pi}{\tilde{T}} - \frac{2\pi}{T} \right)^2 \right\rangle} = \sqrt{\frac{24\Delta t}{\tau^3}} \frac{\sigma}{A}, \tag{43}$$

where $\tilde{T} = 2\pi/\tilde{\omega}$, Δt is the sample interval, and $\tau = N\Delta t$ is the total time, with N being the total number of data points.

C. Rules of data analysis

Generally, the pendulum's frequency ω is subject to external fluctuations (such as the temperature, electrostatic and magnetic fields, air pressure, seismic noise, etc.) and the inherent characteristic of the torsion fiber. In order to obtain the proper period for every data segment and utilize the experimental data to the greatest extent, a standard rule with nine steps has been developed to analyze the angle-time data and finally to obtain the pendulum's periods:

(1) Pretreat the original data. The original signals from the hard disks of the two PCs, including the pendulum twist Δ/Σ, the environmental data, and the time sequence, are combined into one data segment for each near and far position. Then, the pendulum twist Δ/Σ is used as a reference, the data segment between the first and last peaks of Δ/Σ is intercepted, and the initial phase of the pendulum is set as $\phi_0 \approx 0$. The pretreated data are recorded as a $\{t_i, \theta_i, T_{\mathrm{emi}}, \ldots\}$ sequence for subsequent analysis, where t_i, θ_i, and T_{emi} are the time, rotational angle, and temperature at the ith sample, respectively.

(2) Determine the reference frequency ω_r. A discrete fast Fourier transform analysis is performed on the angle-time sequence $\{t_i, \theta_i\}$ to determine the fundamental frequency of the pendulum approximatively. This frequency is set as the value of ω_r to create the standard reference sequences $\{\cos(\omega_r t_i)\}$ and $\{\sin(\omega_r t_i)\}$.

(3) Calculate the phase difference $\{\phi_j\}$ between the pendulum's angle-time sequence and the standard reference signal according to Eq. (39).

(4) Reject data polluted by external disturbances, such as sudden disturbances from the seismic noise and local electromagnetic field, small pressure bursts in vacuum chamber, etc. We exclude the bad data from our final analysis by examining the difference in phase and using the 3σ criterion in the sequence $\Delta\phi_j = \phi_j - \phi_{j-1}$. The polluted oscillation period usually has a sharp burst in $\Delta\phi_j$. Further, the polluted phase (such as ϕ_m) is replaced by a new value: $\phi_m = \phi_0 + \sum_{i=1}^{m} \Delta\phi_i$.

(5) Determine the angle θ_0 and oscillation amplitude A in each full period. The equilibrium position and amplitude of the pendulum in each full oscillation are evaluated by using the reference frequency ω_r as

$$\bar{\theta}_j = \frac{1}{T_r} \int_{jT_r}^{(j+1)T_r} \theta(t) dt, \tag{44}$$

and

$$\bar{A}_j = \left[\left(\frac{2}{T_r} \int_{jT_r}^{(j+1)T_r} \theta(t) \sin(\omega_r t) dt \right)^2 + \left(\frac{2}{T_r} \int_{jT_r}^{(j+1)T_r} \theta(t) \cos(\omega_r t) dt \right)^2 \right]^{1/2}. \tag{45}$$

The real-time angle between the center line of the source masses and the equilibrium position of the pendulum $\{\theta_{0i} = \bar{\theta}_i - \theta_0\}$ and the amplitude of the pendulum $\{\bar{A}_i\}$ are obtained to correct the gravitational nonlinear effect subsequently.

(6) Correct the thermoelastic effect. By using the thermoelastic coefficient of $\alpha_k = -145(2) \times 10^{-6}/^{\circ}\mathrm{C}$ measured in Sec. IV B 2, the period T at the temperature $\mathcal{T}_i$ is corrected to $[T_0 + \alpha_k(\mathcal{T}_i - \mathcal{T}_r)]$, where T_0 is the period at the reference temperature $\mathcal{T}_r = 20.20\,^{\circ}\mathrm{C}$. The average temperature change in the jth period is

$$\langle \mathcal{T}_j \rangle \equiv \int_{jT_r}^{(j+1)T_r} \frac{\mathcal{T}(t) - \mathcal{T}_0}{T_r} dt. \tag{46}$$

The phase after correction for the thermoelastic effect can be written as

$$\tilde{\phi}_j = \phi_j - \frac{2\pi}{T_r} \alpha_k \sum_{i=0}^{j} \langle \mathcal{T}_i \rangle. \tag{47}$$

(7) Correct the gravitational nonlinear effect. The correction to the phase is obtained by integrating ω in Eq. (32) over time. By using the gravitational nonlinear coefficient K_{3g} calculated in Sec. IV C, and taking $\{\bar{\theta}_{0i}\}$ and $\{\bar{A}_i\}$ into account, the phase is changed to

$$\varphi_j = \tilde{\phi}_j + \frac{T_r^2}{2\pi I}\sum_{i=0}^{j}\left(\frac{3}{8}K_{3g}\bar{A}_i^2 + \frac{3}{2}K_{3g}\bar{\theta}_{0i}^2\right). \quad (48)$$

(8) Determine the period of the pendulum for each data segment. By performing a quadratic polynomial fitting to the obtained φ_j, a slope κ at the midpoint in time is obtained. The period at the midpoint of each data segment T_j is

$$T_j = T_r + \kappa\frac{T_r}{2\pi}. \quad (49)$$

Thus the time-period sequence of each data segment $\{t_j, T_j\}$ is obtained.

(9) Remove the exponential aging effect of the fiber, as discussed in Sec. IV B 4. The time-period sequence $\{t_j, T_j\}$ at the near and far positions is used to perform a simultaneous fit:

$$\begin{aligned} T_n(t) &= T_{n,i} + \delta T(1 - e^{-b_W t}), \\ T_f(t) &= T_{f,i} + \delta T(1 - e^{-b_W t}), \end{aligned} \quad (50)$$

where b_W and δT are constant within each experiment. After removing the exponential aging effect, we obtain a new time-period sequence $\{t_i, T_i\}$. Table VI lists the time-period sequence for experiment I, which includes ten sets of data with the source masses alternately at the near and far positions and four sets of background data without the source masses. Table VII lists the time-period sequence for experiment II, which includes six sets of background data without the source masses and seven sets of data with the source masses.

The accuracy of the starting point in time sequence $\{t_i\}$ is better than 10 s, which is determined by the PC's clock, and contributes an uncertainty of only 0.01 ppm to the final G value. The period T_i at t_i extracted by the above steps has uncertainties of ~0.01 ms [86], which is 4–5 times larger than that predicted by Eq. (43) but greatly smaller than the standard deviation of the periods in a 3-day data set due to the aging effect of the torsion fiber. It means that the dominant source of noise is not the intrinsic noise but the bigger external noise.

D. Determine $\Delta\omega^2$ with "*A-B-A*" method

The time-period sequence $\{t_j, T_j\}$ obtained in experiments I and II is shown in Fig. 42 and 43, respectively. Because of the linear aging effect of the torsion fiber, as well as the inhomogeneous background gravitational gradient, a long-term drift of the period at a uniform rate of ~ -0.5 ms/day for both near and far positions is observed in both experiments. To obtain the $\Delta\omega^2$ between the two positions, the so-called *A-B-A* method is used to reduce the effect of the uniform long-term drift of the periods.

TABLE VI. Time-period sequence $\{t_j, T_j\}$ in experiment I.

Set	Starting date	Position	Time t_i (day)	Period T_i (s)
With the source masses:				
1-1	20070321	Far	1.882 91	535.809 80
1-2	20070324	Near	4.806 97	532.560 28
2-1	20070327	Far	7.846 11	535.805 57
2-2	20070330	Near	10.862 96	532.555 79
3-1	20070403	Far	14.829 86	535.800 66
3-2	20070406	Near	17.846 78	532.551 22
4-1	20070409	Far	20.858 18	535.797 11
4-2	20070412	Near	23.828 63	532.547 97
5-1	20070416	Far	27.820 00	535.792 96
5-2	20070419	Near	30.254 18	532.544 38
6-1	20070422	Far	33.820 73	535.790 59
6-2	20070425	Near	36.800 13	532.541 98
7-1	20070428	Far	39.792 23	535.787 66
7-2	20070501	Near	42.861 64	532.538 98
8-1	20070504	Far	45.887 88	535.784 97
8-2	20070507	Near	48.907 76	532.536 06
9-1	20070511	Far	52.831 47	535.781 80
9-2	20070514	Near	55.832 65	532.533 82
10-1	20070517	Far	58.890 21	535.779 85
10-2	20070520	Near	61.903 83	532.531 28
Without the source masses:				
1-1	20080419	Near	1.805 04	535.172 46
1-2	20080422	Far	4.859 07	535.170 48
2-1	20080425	Near	7.854 33	535.169 33
2-2	20080428	Far	10.824 59	535.168 30
3-1	20080501	Near	13.807 17	535.167 16
3-2	20080504	Far	16.802 27	535.166 16
4-1	20080507	Near	19.791 13	535.165 09
4-2	20080510	Far	22.343 28	535.164 20

By using a linear interpolation, $\Delta\omega_i^2$ is determined by the adjacent three periods (near-far-near or vice versa) and the corresponding time sequence $\{t_i\}$. This yields

$$\Delta\omega_i^2 = (-1)^i\left\{\left[\omega_{i-1}^2(t_{i-1})\frac{t_{i+1} - t_i}{t_{i+1} - t_{i-1}} + \omega_{i+1}^2(t_{i+1}) \times \frac{t_i - t_{i-1}}{t_{i+1} - t_{i-1}}\right] - \omega_i^2(t_i)\right\}, \quad (51)$$

where $i = 2, 3, \ldots, 2n - 1$, with n being the number of data sets. Each data set includes one near and one far position. Further, $\Delta\omega^2$ is determined by

$$\Delta\omega^2 = \frac{1}{2n - 2}\sum_{i=2}^{2n-1}\Delta\omega_i^2. \quad (52)$$

TABLE VII. Time-period sequence $\{t_j, T_j\}$ in experiment II.

Set	Starting date	Position	Time t_i (day)	Period T_i (s)
Without the source masses:				
1-1	20080825	Far	1.801 57	535.251 29
1-2	20080828	Near	4.831 06	535.247 05
2-1	20080831	Far	7.838 87	535.245 37
2-2	20080903	Near	10.818 87	535.243 03
3-1	20080906	Far	13.674 84	535.242 06
3-2	20080910	Near	17.343 76	535.239 60
4-1	20080913	Far	20.385 00	535.238 65
4-2	20080916	Near	23.383 68	535.237 36
5-1	20080919	Far	26.372 96	535.236 90
5-2	20080922	Near	29.365 18	535.235 71
6-1	20080925	Far	32.373 15	535.236 00
6-2	20080928	Near	35.378 62	535.235 00
With the source masses:				
1-1	20081008	Near	1.870 30	532.841 27
1-2	20081011	Far	4.898 27	536.071 02
2-1	20081014	Near	7.871 53	532.832 46
2-2	20081017	Far	10.869 52	536.064 99
3-1	20081020	Near	13.866 48	532.838 18
3-2	20081023	Far	16.869 57	536.061 52
4-1	20081026	Near	19.842 24	532.824 85
4-2	20081029	Far	22.882 87	536.059 07
5-1	20081101	Near	25.893 01	532.823 11
5-2	20081104	Far	28.883 97	536.057 55
6-1	20081107	Near	31.875 10	532.821 67
6-2	20081110	Far	34.884 81	536.056 22
7-1	20081113	Near	37.839 07	532.820 34
7-2	20081116	Far	40.879 42	536.054 92

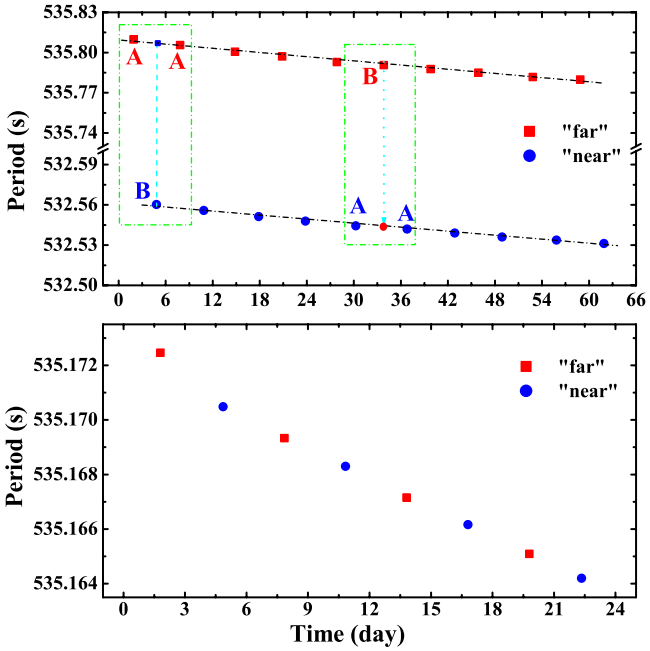

FIG. 42 (color online). Upper: The period versus time extracted from ten sets of angle-time data with the source masses at the near and far positions alternately in experiment I. The circle and square points represent the pendulum's period at the near and far positions, respectively. The dashed lines with the same slope reveal a linear drift of the pendulum's period. Lower: The period versus time for four sets of background data without the source masses. The *A-B-A* method is shown in this figure.

Since

$$\frac{t_{i+1} - t_i}{t_{i+1} - t_{i-1}} \approx \frac{t_i - t_{i-1}}{t_{i+1} - t_{i-1}} \approx 1/2, \tag{53}$$

Eq. (52) reduces to

$$\Delta\omega^2 = \frac{1}{2n-2}\left(\frac{1}{2}\omega_1^2 - \frac{3}{2}\omega_2^2 + 2\omega_3^2 + \cdots\right). \tag{54}$$

The statistical uncertainty of $\Delta\omega^2$ becomes

$$u[\Delta\omega^2] = \frac{\sigma_{[\Delta\omega_i^2]}}{\sqrt{n}}, \tag{55}$$

assuming that the standard deviation $\sigma_{[\Delta\omega_i^2]}$ remains constant as $n \to \infty$. The values of $\Delta\omega^2$ obtained in the two experiments are listed in Table VIII. The final $\Delta\omega^2$ is obtained from

$$\Delta\omega^2 = \Delta\omega_{nf}^2 - \Delta\omega_{\text{back}}^2, \tag{56}$$

where $\Delta\omega_{nf}^2$ is the difference of the frequency squared with the source masses at the near and far positions alternately and $\Delta\omega_{\text{back}}^2$ is that without the source masses. The uncertainty of $\Delta\omega^2$ is obtained directly by adding those of $\Delta\omega_{nf}^2$

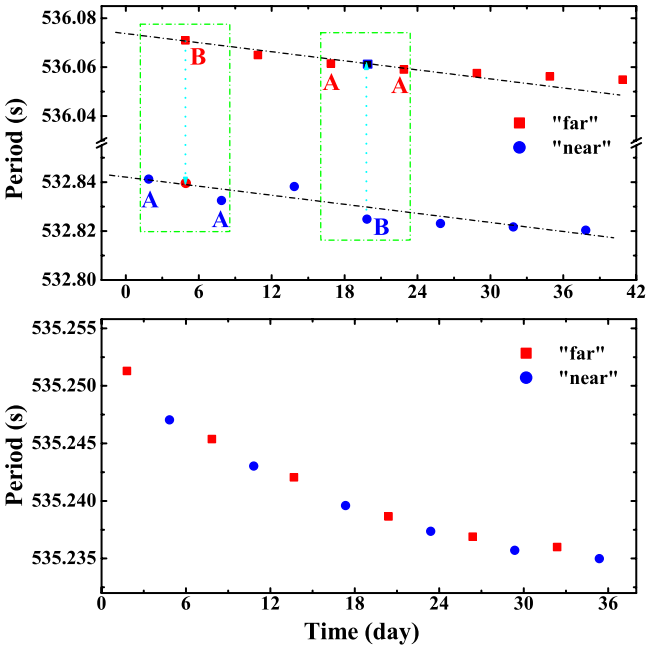

FIG. 43 (color online). The period versus time in experiment II from seven sets of data with the source masses and six sets without the source masses. Notations are the same as for Fig. 42.

TABLE VIII. Determined $\Delta\omega^2$ in units of 10^{-6} s^{-2}.

Parameter	Experiment I	Experiment II
$\Delta\omega^2_{nf}$	1.682 275(29)	1.673 407(15)
$\Delta\omega^2_{\text{back}}$	0.000 030(12)	0.000 272(36)
$\Delta\omega^2$	1.682 245(31)	1.673 135(39)

and $\Delta\omega^2_{\text{back}}$ quadratically, which yields $u_r = 18.43$ and 23.31 ppm in experiment I and II, respectively.

VI. EXPERIMENTAL RESULTS

Substituting all the measured parameters mentioned above into Eq. (7), we obtain two G values from experiments I and II:

$$G1 = (6.673\,52 \pm 0.000\,19) \times 10^{-11}\ \text{m}^3\,\text{kg}^{-1}\,\text{s}^{-2},$$
$$G2 = (6.673\,46 \pm 0.000\,21) \times 10^{-11}\ \text{m}^3\,\text{kg}^{-1}\,\text{s}^{-2}. \quad (57)$$

The uncertainties of the two G values are 28.86 and 32.17 ppm, respectively. The value of $G2$ is 9.0 ppm smaller than $G1$, half of which is chosen as the error entirely due to the density inhomogeneity of the two source masses. By averaging the two G values and taking the correlations of the uncertainties in the two experiments into account, the combined final value of G is found to be

$$G = (6.673\,49 \pm 0.000\,18) \times 10^{-11}\ \text{m}^3\,\text{kg}^{-1}\,\text{s}^{-2} \quad (58)$$

with a combined uncertainty of 26.33 ppm [27].

The complete 1σ error budget in determining G is listed in Table IX. For the present G value, the main uncertainty is from the anelastic effect of the torsion fiber used, which brings in a correction of -211.80 ppm to our G value and contributes an uncertainty of 18.69 ppm. The main limit in the precision comes from reloading the pendulum frequently to exchange the two disk pendulums, as discussed in Ref. [91]. In determining $\Delta C_g/I$, the distance between the GCs of the two spheres contributes the dominant uncertainty to the G value in the two experiments through the nonsphericities of the spheres. Compared with experiment I, a smaller correction of the thermoelastic effect occurred in experiment II because the experimental temperature is more close to the reference temperature 20.20 °C, and a smaller correction of the gravitational nonlinear effect of the source masses is necessary in experiment II due to the 209-μm larger spherical center distance, smaller angle θ_0, and smaller oscillating amplitude A. The magnetic damper in the two-stage pendulum system also introduces a correction of 17.54 ppm and an uncertainty of only 0.31 ppm. Another large error from the statistical $\Delta\omega^2$, 18.43 and 23.31 ppm in experiment I and II, respectively, is chiefly due to the fluctuation of the pendulum's period caused by the external noise and the nonconstant characters of the torsion fiber.

TABLE IX. The complete 1σ error budget in determining G. The values in the square brackets are for experiment II distinctively.

Error sources	Corrections (ppm)	$\delta G/G$ (ppm)
Torsion pendulum		5.05 [5.05]
Dimension		1.95
Attitude		0.13 [0.07]
Density inhomogeneity		<0.21
Chamfer property		0.34
Three chips	−0.12	0.17
Coating layer	−24.28	4.33
Clamp and ferrule		1.65
Reflecting mirror		0.03
Source masses		10.66 [10.64]
Masses		0.82
Distance of GCs		9.64 [9.61]
Density inhomogeneity		4.50
Relative positions		1.10 [1.31]
Height of pendulum		0.76 [0.40]
Height of spheres		0.48 [0.27]
Position of torsion fiber		0.63 [1.22]
Position of turntable		0.05
θ_0		0.06 [0.01]
Fiber		18.76
Nonlinearity		<0.70
Thermoelasticity	−39.83 [8.37]	1.52 [0.82]
Anelasticity	−211.80	18.69
Aging		<0.01
Gravitational nonlinearity	7.73 [4.79]	0.30 [0.20]
Magnetic damper	17.54	0.31
Magnetic field		0.40
Electrostatic field		0.10
Statistical $\Delta\omega^2$		18.43 [23.31]
Total		28.86 [32.17]
Combined		26.33

VII. DISCUSSIONS

The absolute value of the Newtonian gravitational constant G was determined by using the classical time-of-swing method with a torsion pendulum. Several improvements, over our previous G measurement [19,28], greatly reduced the uncertainties in the present result. First, the cylindrical source masses were replaced by the spheres, which proved to have more homogeneous density and smaller offsets of the CM from GC. Second, the simple rectangular glass pendulum has fewer vibration modes and hence improved the stability of the period and reduced the metrological uncertainties. Third, the measurements of the relative positions and alignments between the pendulum and the source masses became more convenient and precise because all set in the vacuum chamber. Besides, with all the masses in the same vacuum chamber, we can ignore the effect of the air density, which caused a 150-ppm correction in our previous experiment due to omitting the effect of the air buoyancy [19]. Fourth, the near and far

positions were switched remotely by using a stepper motor, which indeed lowered the environmental disturbances, especially the thermal and gravitational effects due to the experimenter's presence. Last, the anelastic effect of the torsion fiber was first measured directly by using two disk pendulums with the help of a high-Q quartz fiber. Even though it is still responsible for the largest uncertainty in the present G value, the independent measurement of the anelasticity assured us that our present G value is immune to a big correction.

What is the most significant in the present G measurement is that the two experiments were performed by three subgroups which were "blind" to one another. Two subgroups performed the measurements independently, and the third subgroup carried out the data analysis with the same procedures but without knowing the accurate dimensions of the pendulum. After all the measurements and most of the data analysis were finished, the envelope containing the pendulum's dimensions was opened, the pendulum's dimensions were put in, and our G values came out.

The present G value agrees with the value determined in HUST-05 of $6.6723(9) \times 10^{-11}$ $\mathrm{m^3\,kg^{-1}\,s^{-2}}$ [19] in 2σ, which is corrected from the HUST-99 result by a fractional increase of 360 ppm due to the offsets of the CM of the source masses (210 ppm) as well as the effect of the air buoyancy (150 ppm). Figure 44 compares the present G values from experiments I and II and their combination with the other measurements with uncertainties better than 50 ppm [20,21,23,26] and the CODATA 2002 and 2006 [15,16]. The present G value is smaller than the CODATA 2006 recommended value by a fractional amount of 118 ppm, slightly larger than the uncertainty 100 ppm assigned to the CODATA 2006 value. Comparison between our two G values and the CODATA recommended values of G from 1973 to 2006 is shown in Fig. 45.

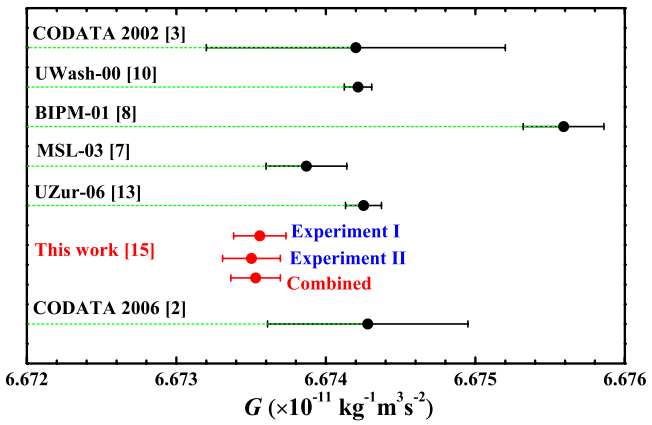

FIG. 44 (color online). Comparison between our present G values and other results with uncertainties better than 50 ppm [20,21,23,26], as well as the CODATA 2002 and 2006 recommended values [15,16].

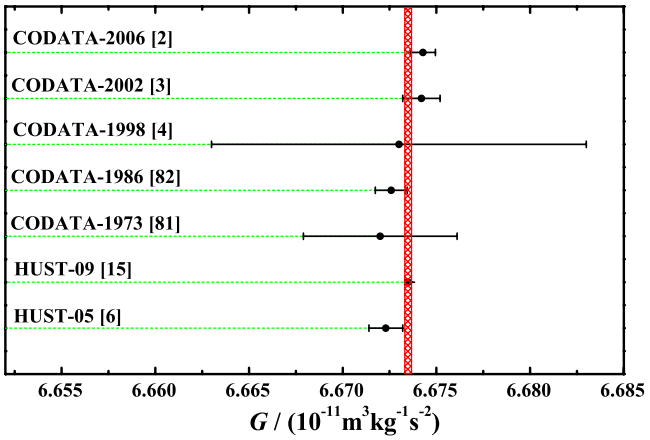

FIG. 45 (color online). Comparison between our G values (HUST-05 and 09) and the CODATA recommended values from 1973 to 2006 [15–17,102,103]. The width of the gridding region shows our present G value with $\pm 1\sigma$ uncertainty.

The G values in Fig. 44 are still in poor agreement. This encourages us to perform better G measurements. We plan to measure G by using two methods to find the possible unknown systematic uncertainties in the present G measurements. One scheme will use the time-of-swing method where two kinds of torsion fibers (a pure tungsten fiber and a quartz fiber) with different Q will be used. Our preliminary experiment shows that the pendulum suspended by a pure tungsten fiber and a quartz fiber with 25-μm diameter had Q's of $\sim$3000 and $\sim$100 000, respectively, which will help us to improve the stability of the pendulum's period especially for the quartz fiber with high Q. Besides, the G values obtained by using fibers with two different Q's will provide an indirect test of the anelasticity of the fiber in the time-of-swing method. However, the problem related to the electrostatic interactions will be the major challenge in using the quartz fiber. Recent reports [97,98] that the metal-coated fused silica fiber still has a high Q give us confidence to use the quartz fiber to perform future G measurements. The other scheme will use the angular acceleration feedback method, which was proposed by Rose *et al.* [99] and developed by Gundlach *et al.* [100,101], who obtained a G value [23] with the smallest uncertainty up to now. The major advantage of this method is that it will reduce the dependence on many properties of the torsion fiber.

Besides, several technical improvements will be made, which aim at the big corrections in the error budget in Table IX and improve the stability of the pendulum's period. A copper tube with high thermal conductivity will be used to surround the main torsion fiber in the vacuum chamber to provide a constant temperature environment, which could further lower the thermoelastic uncertainty of the torsion fiber. The gravity gradient of the experimental location will be compensated, as described in Ref. [91], to achieve a more homogeneous gravitational

background at the location of the pendulum. This will help us to improve the linear drift of the pendulum's period. Besides, the gold-coated layer of the pendulum will be replaced by a thinner aluminum-coated layer due to its lower density. We will continue to use spherical source masses in our future G measurements, and the position and the orientation of the spheres will be changed several times in order to average out density fluctuations and nonsphericity. The prospective uncertainties of the two G values by the two methods will be both less than 20 ppm.

ACKNOWLEDGMENTS

We spent about ten years to prepare and perform the present experiments, and many people provided a great deal of help during the course of our G measurements. We are grateful to Riley Newman of University of California, Irvine, Ho Jung Paik of University of Maryland, Vadim Milyukov of Sternberg State Astronomical Institute of Moscow State University, Kazuaki Kuroda of University of Tokyo, and Zhong-Zhu Liu and Ze-Bing Zhou in our laboratory for their valuable discussions and suggestions. We thank Mr. Liang Zhao and many others for their preliminary research work in the G measurement as master graduate students in our laboratory. Many thanks go to Mrs. Yan Chen of Measurement Institute of Jiujiang for grinding and polishing the source masses with great care and endurance over two years. The National Institute of Metrology of China provided all certification reports on the length of the gauges and the vacuum mass of the spheres. The Center for Analysis and Testing of Huazhong University of Science and Technology provided the FEI-Quanta 200 SEM for us to sample the density inhomogeneity of the spherical source masses. This work is supported in part by the National Basic Research Program of China under Grant No. 2010CB832801, the National High-Tech Research and Development Plan of China under Grant No. 2008AA12A215, and the National Natural Science Foundation of China under Grant No. 10805021.

APPENDIX A: THE MATHEMATICAL MODELING OF G

For a two-stage pendulum system shown in Fig. 2, the Lagrangian of the torsion pendulum system can be written as

$$L = \tfrac{1}{2}I_m\dot{\theta}_m^2 + \tfrac{1}{2}I\dot{\theta}^2 - \tfrac{1}{2}K_m\theta_m^2 - \tfrac{1}{2}K(\theta - \theta_m)^2 - V_g(\theta), \tag{A1}$$

where I_m, I, K_m, and K are defined in Fig. 2, and θ_m and θ are the rotation angles of the prehanger fiber and the main torsion fiber relative to their equilibrium positions, respectively. $V_g(\theta)$ is the gravitational potential between the pendulum and the source masses, and the gravitational spring constant K_g is the second derivative of $V_g(\theta)$. Here $V_g(\theta_m) \approx 0$ because the magnetic damper is a symmetrical circular disk and the ΔC_{gm} contributed by the magnetic damper is zero between the near and far positions.

By substituting Eq. (A1) into the Lagrange equation, the equations for the torsional modes are found:

$$\begin{aligned} I_m\ddot{\theta}_m + K_m\theta_m - K(\theta - \theta_m) = 0, \\ I\ddot{\theta} + K(\theta - \theta_m) + K_g\theta = 0. \end{aligned} \tag{A2}$$

By substituting trial solutions $\theta_m = A_m e^{i\omega t}$ and $\theta = Ae^{i\omega t}$ to Eq. (A2), one obtains

$$\begin{aligned} (K_m + K - I_m\omega^2)A_m - KA = 0, \\ -KA_m + (K + K_g - I\omega^2)A = 0. \end{aligned} \tag{A3}$$

To have a solution, Eq. (A3) must satisfy

$$\begin{vmatrix} K_m + K - I_m\omega^2 & -K \\ -K & K + K_g - I\omega^2 \end{vmatrix} = 0, \tag{A4}$$

i.e.,

$$K_g = I\omega^2 - K + \frac{K^2}{K_m + K - I_m\omega^2}. \tag{A5}$$

At the near and far positions, Eq. (A5) can be expressed as

$$K_{gn} = GC_{gn} = I\omega_n^2 - K(\omega_n) + \frac{K^2(\omega_n)}{K_m + K(\omega_n) - I_m\omega_n^2}, \tag{A6}$$

$$K_{gf} = GC_{gf} = I\omega_f^2 - K(\omega_f) + \frac{K^2(\omega_f)}{K_m + K(\omega_f) - I_m\omega_f^2}, \tag{A7}$$

where the subscripts n and f denote the near and far positions, respectively, and C_{gn} and C_{gf} are defined in the text and determined by the mass distributions of the pendulum and source masses.

By using Eqs. (A6) and (A7), and defining $\Delta(\omega^2) = \omega_n^2 - \omega_f^2$ and $\Delta K(\omega) = K(\omega_n) - K(\omega_f)$, G can be expressed as

$$G = \frac{1}{\Delta C_g}\left\{I\Delta(\omega^2) - \Delta K(\omega) + \frac{K^2(\omega_n)}{K_m + K(\omega_n) - I_m\omega_n^2} \times \left[1 - \frac{K^2(\omega_f)}{K^2(\omega_n)}\frac{1}{1 + \frac{I_m\Delta(\omega^2) - \Delta K(\omega)}{K_m + K(\omega_n) - I_m\omega_n^2}}\right]\right\}. \tag{A8}$$

The main parameters of the two-stage pendulum system in our G measurement are $K_m = 1.030(8) \times 10^{-6}$ N m rad^{-1}, $I_m = 2.180(14) \times 10^{-5}$ kg m^2, $K = 6.175(2) \times 10^{-9}$ N m rad^{-1}, $I = 4.450(1) \times 10^{-5}$ kg m^2, $\omega_n^2 = 1.395 \times 10^{-4}$ s^{-2} (the period of the pendulum at the near position is 532.8 s), and $\Delta(\omega^2) = 1.682 \times 10^{-6}$ s^{-2}. Linear expansion of Eq. (A8) to the first order yields the final expression of G in our experiment as

$$G = \frac{I\Delta(\omega^2)}{\Delta C_g}\left[1 - \frac{\Delta K(\omega)}{I\Delta(\omega^2)} + \frac{I_m K^2(\omega_n)}{IK_m^2}\right], \tag{A9}$$

where the second term in the square brackets denotes the correction for the fiber's anelasticity, and the last term is the correction from the magnetic damper in the two-stage pendulum system.

APPENDIX B: CALCULATING $\Delta C_g/I$

1. General principle

In the laboratory coordinate system (X, Y, Z), as defined in Sec. II B, the gravitational potential between the pendulum and one of the spheres (sphere 2) is

$$V_g = -GM\int \frac{\rho_p dxdydz}{\sqrt{(X_2 - x)^2 + (Y_2 - y)^2 + (Z_2 - z)^2}}, \tag{B1}$$

where M is the mass of sphere 2, ρ_p is the density of the pendulum, (X_2, Y_2, Z_2) is the center of the sphere, and (x, y, z) is the point mass in the pendulum. The integral is over the volume of the pendulum. The second derivative of the gravitational potential $V_g(\theta)$ evaluated at $\theta = 0$ yields the gravitational spring constant K_g, which is related to G as

$$K_g = GC_g = \frac{\partial^2 V_g(\theta)}{\partial\theta^2}\bigg|_{\theta=0}. \tag{B2}$$

Substituting Eq. (B1) into Eq. (B2), we get the gravitational coupling coefficient C_g:

$$C_g = -M\int \Gamma|_{\theta=0} dxdydz, \tag{B3}$$

where Γ is a function of the geometrical and positional parameters, which can be expressed in general as

$$\Gamma = \frac{\partial^2}{\partial\theta^2} F(x, y, z, X_2, Y_2, Z_2, \rho_p, \theta). \tag{B4}$$

Similarly, the inertial moment of the pendulum in the laboratory coordinate system is expressed in general as

$$I_p = \int \rho_p(x^2 + y^2) dxdydz. \tag{B5}$$

2. Pendulum coordinate system (X_0, Y_0, Z_0)

The integration limits for Eqs. (B3) and (B5) are very difficult to determine precisely in the laboratory coordinate system, because the actual pendulum is not an ideal flat plane and its attitude is not perfectly horizontal. Therefore, we introduce another coordinate system fixed on the pendulum, in which the limits of integration will be straightforward and the integrals of ΔC_g and I_p are performed. Then the results are found in the laboratory coordinate system by performing a coordinate transformation.

We define the pendulum frame (X_0, Y_0, Z_0) being approximately parallel to the laboratory coordinate system. The origin O_0 of the pendulum frame is at the GC of the pendulum, and its coordinates in the laboratory frame are $(\delta X, \delta Y, \delta Z)$ because the origin O of the laboratory frame is the CM of the pendulum. The vertical Z_0 axis points up along the pendulum's height direction, and the horizontal X_0 axis is along the pendulum's length.

3. The coordinate transformation

The attitude of the pendulum is defined by angles α and β about the X and Y axes in the laboratory frame, respectively, and the pendulum coordinate system can be obtained from the laboratory frame by performing operations of rotation and translation successively.

The unit vectors of the laboratory frame and the pendulum frame are $(\mathbf{i}, \mathbf{j}, \mathbf{k})$ and $(\mathbf{e}_x, \mathbf{e}_y, \mathbf{e}_z)$, respectively. The two sets of the unit vectors are set to point along the same directions originally. The practical attitude of the pendulum could be obtained from the laboratory frame by performing the following operations. First, rotating the pendulum frame by α and β about the X and Y axes, respectively, changes the unit vectors of the pendulum frame into $(\mathbf{e}_{x2}, \mathbf{e}_{y2}, \mathbf{e}_{z2})$. Under the approximation of $\alpha = \Delta\theta_X$ and $\beta = \Delta\theta_Y$, which are measured directly in Sec. II E 7, we obtain

$$\begin{pmatrix}\mathbf{e}_{x2}\\ \mathbf{e}_{y2}\\ \mathbf{e}_{z2}\end{pmatrix} = \begin{pmatrix}\cos\beta & 0 & -\sin\beta\\ \sin\alpha\sin\beta & \cos\alpha & \cos\beta\sin\alpha\\ \cos\alpha\sin\beta & -\sin\alpha & \cos\alpha\cos\beta\end{pmatrix}\begin{pmatrix}\mathbf{i}\\ \mathbf{j}\\ \mathbf{k}\end{pmatrix}. \tag{B6}$$

Then, the pendulum is rotated about the torsion fiber by θ, which rotates the unit vectors of the pendulum frame once more into $(\mathbf{e}_x, \mathbf{e}_y, \mathbf{e}_z)$:

$$\begin{pmatrix}\mathbf{e}_x\\ \mathbf{e}_y\\ \mathbf{e}_z\end{pmatrix} = \Re\begin{pmatrix}\mathbf{i}\\ \mathbf{j}\\ \mathbf{k}\end{pmatrix}, \tag{B7}$$

where the transformation matrix $\Re$ between the two sets of the unit vectors is

$$\Re = \begin{pmatrix}\cos\beta\cos\theta & \cos\beta\sin\theta & -\sin\beta\\ \cos\theta\sin\alpha\sin\beta - \cos\alpha\sin\theta & \cos\alpha\cos\theta + \sin\alpha\sin\beta\sin\theta & \cos\beta\sin\alpha\\ \cos\theta\cos\alpha\sin\beta + \sin\alpha\sin\theta & -\sin\alpha\cos\theta + \cos\alpha\sin\beta\sin\theta & \cos\alpha\cos\beta\end{pmatrix}. \tag{B8}$$

For a point P with coordinates $P(X, Y, Z)$ in the laboratory frame and $P(X_0, Y_0, Z_0)$ in the pendulum frame, we have

$$\begin{pmatrix} X \\ Y \\ Z \end{pmatrix} = \Re^T \begin{pmatrix} X_0 \\ Y_0 \\ Z_0 \end{pmatrix} + \begin{pmatrix} \delta X \\ \delta Y \\ \delta Z \end{pmatrix}. \tag{B9}$$

Because the CM of the pendulum is $O(\delta X_0, \delta Y_0, \delta Z_0)$ in the pendulum frame and $O(0, 0, 0)$ in the laboratory frame, respectively, we have

$$\begin{pmatrix} 0 \\ 0 \\ 0 \end{pmatrix} = \Re^T \begin{pmatrix} \delta X_0 \\ \delta Y_0 \\ \delta Z_0 \end{pmatrix} + \begin{pmatrix} \delta X \\ \delta Y \\ \delta Z \end{pmatrix}. \tag{B10}$$

Substituting Eq. (B10) into Eq. (B9), we obtain the final expression for the coordinate transformation between (X, Y, Z) and (X_0, Y_0, Z_0):

$$\begin{pmatrix} X \\ Y \\ Z \end{pmatrix} = \Re^T \begin{pmatrix} X_0 - \delta X_0 \\ Y_0 - \delta Y_0 \\ Z_0 - \delta Z_0 \end{pmatrix}. \tag{B11}$$

4. Calculation of I and C_g

According to Eq. (B11), the function $\Gamma(x, y, z)$ in Eq. (B4) is transformed into $\Gamma(x_0, y_0, z_0)$ by using $\Re^T$ transformation matrix. The gravitational coupling coefficient then becomes

$$C_g = -M \int_{-L/2}^{L/2} dx_0 \int_{-W/2}^{W/2} dy_0 \int_{-H/2}^{H/2} dz_0 \cdot \rho_p \Gamma(x_0, y_0, z_0)|_{\theta=0} \left| \frac{\partial(X, Y, Z)}{\partial(X_0, Y_0, Z_0)} \right|, \tag{B12}$$

where L, W, and H represent the length, width, and height of the pendulum, respectively.

The components of C_g between each part on the pendulum (including the pendulum body, coating layer, chips, clamp, ferrule, mirror, and glues, as discussed in Sec. II C) and the source masses (spheres 2 and 4) can be obtained and summed as

$$\Delta C_g = \sum_i [C_{gn,i} - C_{gf,i}], \tag{B13}$$

where the sum is over all the parts on the pendulum system. Similarly, the moment of inertia of the pendulum in Eq. (B5) can be computed conveniently in the pendulum frame and then converted to the laboratory frame by using Eq. (B11). Finally, the parameter $\Delta C_g/I$ is obtained by numerical integration.

The relative uncertainty introduced by any parameter a to the final G value is evaluated as

$$\left(\frac{\delta G}{G}\right)_{\delta a} = \frac{G(a + \delta a, b, c, \ldots) - G(a, b, c, \ldots)}{G(a, b, c, \ldots)}. \tag{B14}$$

Usually, two different values are obtained from Eq. (B14) for positive and negative values of δa, and the larger one is chosen as the final uncertainty to the G value. This yields the error budget given in Table IV in Sec. II F.

APPENDIX C: THE MATHEMATICAL MODELING OF DIAMETER

According to Fig. 12, the diameter of the sphere is determined by measuring the three surface separations (S_{12}, S_{23}, and S_{13}) individually, and the diameter of sphere 2 is determined by $D_2 = S_{13} - S_{12} - S_{23}$. Figure 46 shows the principle of determining S_{13} (similarly, S_{12} and S_{23}) by rotating a gauge block. For an ideal case [Fig. 46(a)], the surface separation between spheres 1 and 3 would be

$$S_{13} = \frac{L_{13} + R_1 + R_3}{\cos\theta} - R_1 - R_3, \tag{C1}$$

where L_{13} is the length of the gauge block used, R_1 and R_3 are the radii of spheres 1 and 3, respectively, and θ is half of

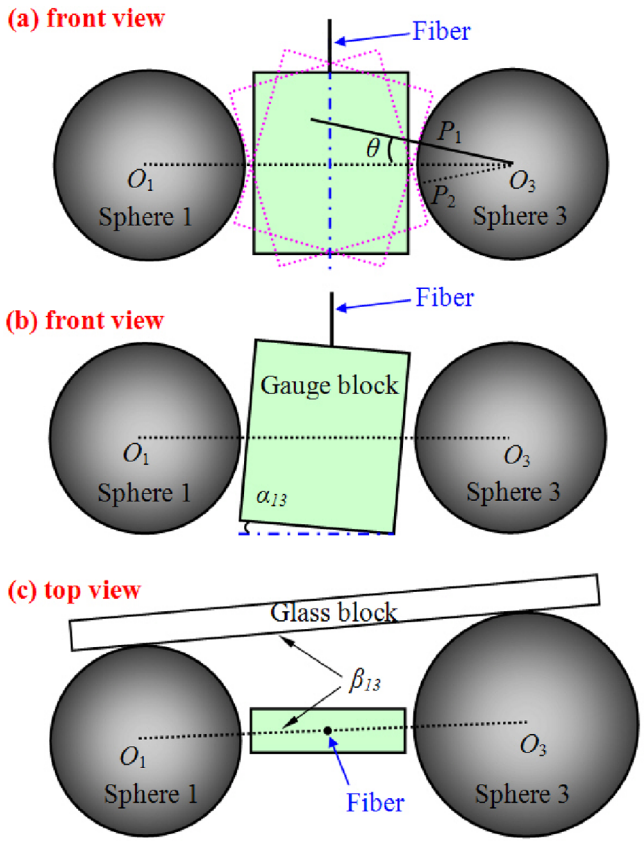

FIG. 46 (color online). The principle of determining surface separation. (a) Ideal case, front view: The solid rectangle denotes the gauge block suspended freely by the torsion fiber, and the two dotted rectangles represent the gauge block touching the two spheres in two different ways, at points P_1 and P_2 with sphere 3. (b) Practical case, front view: The suspended gauge block is not precisely vertical and is tilted by an angle of α_{13}. (c) Practical case, top view: Because of a small difference in diameters, there is an angle β_{13} between the center line of the spheres O_1O_3 and the glass block, which is leaning against the two spheres.

the angle that the gauge could rotate between the two spheres.

In practice, the attitude of the suspended gauge block is tilted by α_{13} [Fig. 46(b)]. Furthermore, the small difference in the diameters of the two spheres causes an angle β_{13} between the center line of the two spheres and the surface of the glass block which is leaning against the two spheres [Fig. 46(c)]. The surface separation in Eq. (C1) is now modified to

$$S_{13} = \frac{(L_{13} + R_1 + R_3)\cos\alpha_{13}}{\cos\theta\cos\beta_{13}} - R_1 - R_3. \tag{C2}$$

By taking into account the correction from temperature, the complete expression of the surface separation S^r_{13} at the temperature $\mathcal{T}_r = 20.20\,^\circ\mathrm{C}$ is found to be

$$\begin{aligned} S^r_{13} = {} & \frac{L_{13}[1 + \alpha_g(\mathcal{T} - \mathcal{T}_g)]\cos\alpha_{13}}{\cos\theta\cos\beta_{13}} \\ & + (R_1 + R_3)\Bigg\{\alpha_s(\mathcal{T}_s - \mathcal{T}_r) - 1 \\ & + \frac{[1 + \alpha_s(\mathcal{T} - \mathcal{T}_s)]\cos\alpha_{13}}{\cos\theta\cos\beta_{13}}\Bigg\}, \end{aligned} \tag{C3}$$

where $\mathcal{T}$ is the actual temperature during the measurement, $\mathcal{T}_g$ is the temperature at which the gauge is calibrated for its nominal length L_{13}, $\mathcal{T}_s$ is the temperature at which the spheres have their nominal radii (R_1 and R_3), and α_s and α_g are the thermal expansion coefficients of the spheres and the gauge, respectively.

To obtain the diameter of sphere 2, we should consider the fact that the three center lines of each pair of spheres are not collinear. In the horizontal plane, the angular deviations γ_{12} and γ_{23} of the surface separations S_{12} and S_{23} from S_{13} are measured. In the vertical plane, corresponding angular deviations β_{12} and β_{23} are measured. Finally, the mathematical expression for the diameter of sphere 2 is

$$D_2 = \frac{S^r_{13}}{2}\left[\frac{1}{\cos\beta_{12}\cos\gamma_{12}} + \frac{1}{\cos\beta_{23}\cos\gamma_{23}}\right] - S^r_{12} - S^r_{23}, \tag{C4}$$

where S^r_{12} and S^r_{23} are the surface separations (Fig. 12) at the temperature $\mathcal{T}_r$.

[1] I. Newton, *Philosophiae Naturalis Principia Mathematica ("Mathematical Principles of Natural Philosophy")* (Joseph Streater, London, 1687).
[2] E. G. Adelberger, B. R. Heckel, and A. E. Nelson, Annu. Rev. Nucl. Part. Sci. **53**, 77 (2003).
[3] S. G. Turyshev, Annu. Rev. Nucl. Part. Sci. **58**, 207 (2008).
[4] E. G. Adelberger *et al.*, Prog. Part. Nucl. Phys. **62**, 102 (2009).
[5] P. A. M. Dirac, Nature (London) **139**, 323 (1937).
[6] P. A. M. Dirac, Proc. R. Soc. A **165**, 199 (1938).
[7] S. A. Cook, Rep. Prog. Phys. **51**, 707 (1988).
[8] G. T. Gillies, Rep. Prog. Phys. **60**, 151 (1997).
[9] J. Luo and Z. K. Hu, Classical Quantum Gravity **17**, 2351 (2000).
[10] J. P. Uzan, Rev. Mod. Phys. **75**, 403 (2003).
[11] S. G. Turyshev, Phys. Usp. **52**, 1 (2009).
[12] J. G. Williams, S. G. Turyshev, and D. H. Boggs, Phys. Rev. Lett. **93**, 261101 (2004).
[13] J. G. Williams, S. G. Turyshev, and D. H. Boggs, Phys. Rev. Lett. **98**, 059002 (2007).
[14] H. Cavendish, Philos. Trans. R. Soc. London **88**, 469 (1798).
[15] P. J. Mohr, B. N. Taylor, and D. B. Newell, Rev. Mod. Phys. **80**, 633 (2008).
[16] P. J. Mohr and B. N. Taylor, Rev. Mod. Phys. **77**, 1 (2005).
[17] P. J. Mohr and B. N. Taylor, Rev. Mod. Phys. **72**, 351 (2000).
[18] O. V. Karagioz and V. P. Izmailov, Izmeritel'naya Tekhnika **39**, 3 (1996) [Measurement Techniques **39**, 979 (1996)].
[19] Z. K. Hu, J. Q. Guo, and J. Luo, Phys. Rev. D **71**, 127505 (2005).
[20] T. R. Armstrong and M. P. Fitzgerald, Phys. Rev. Lett. **91**, 201101 (2003).
[21] T. J. Quinn *et al.*, Phys. Rev. Lett. **87**, 111101 (2001).
[22] C. H. Bagley and G. G. Luther, Phys. Rev. Lett. **78**, 3047 (1997).
[23] J. H. Gundlach and S. M. Merkowitz, Phys. Rev. Lett. **85**, 2869 (2000).
[24] U. Kleinevoß, Ph.D. thesis, University of Wuppertal, 2002.
[25] S. Schlamminger, E. Holzschuh, and W. Kundig, Phys. Rev. Lett. **89**, 161102 (2002).
[26] S. Schlamminger *et al.*, Phys. Rev. D **74**, 082001 (2006).
[27] J. Luo *et al.*, Phys. Rev. Lett. **102**, 240801 (2009).
[28] J. Luo *et al.*, Phys. Rev. D **59**, 042001 (1998).
[29] P. R. Heyl, Bur. Stand. J. Res. **5**, 1243 (1930).
[30] P. R. Heyl and P. Chrzanowski, J. Res. Natl. Bur. Stand. **29**, 1 (1942).
[31] M. U. Sagitov *et al.*, Dokl. Akad. Nauk SSSR **245**, 567 (1979) [Sov. Phys. Dokl. **245**, 20 (1981)].
[32] O. V. Karagyoz, A. H. Silin, and V. F. Iszmaylov, Izv. Akad. Nauk SSSR, Fiz. Zemli **17**, 92 (1981) [Izv., Acad. Sci., USSR, Phys. Solid Earth (Engl. Transl.) **17**, 66 (1981)].
[33] G. G. Luther and W. R. Towler, Phys. Rev. Lett. **48**, 121 (1982).
[34] R. D. Newman and M. K. Bantel, Meas. Sci. Technol. **10**, 445 (1999).
[35] L. Zhao *et al.*, Chin. Phys. Lett. **20**, 1206 (2003).
[36] Y. Tu *et al.*, Phys. Lett. A **331**, 354 (2004).

[37] X. D. Fan *et al.*, Phys. Lett. A **372**, 547 (2008).
[38] K. Kuroda, Phys. Rev. Lett. **75**, 2796 (1995).
[39] Goniometer 410, Huber Diffraktionstechnik GmbH, Germany.
[40] 2XZ-8, Chengdu Languang Vacuum Equipment Company, Chengdu, China.
[41] FB-600, KYKY Technology Development Ltd., Beijing, China.
[42] SP-400, Shanghai Shanjin Vacuum Equipment Co., Ltd., Shanghai, China.
[43] S. H. Fan, S. C. Wu, and J. Luo, Rev. Sci. Instrum. **68**, 3079 (1997).
[44] Goodfellow Cambridge Limited, Huntingdon PE29 6WR, England.
[45] LK-0005, BIUPE Nanometer Measurement & Control Co., Ltd., Beijing, China.
[46] CD1K2007-0378, Verification Certificate of National Institute of Metrology, China.
[47] AT-106, Mettler Toledo company, Switzerland.
[48] JVT250, Guiyang Xintian Oetech Co. Ltd., Guizhou, China.
[49] J. H. Gladstone and T. P. Dale, Phil. Trans. R. Soc. London **153**, 317 (1863).
[50] B. Marler, Phys. Chem. Miner. **16**, 286 (1988).
[51] L. X. Liu *et al.*, Chin. Phys. Lett. **25**, 4203 (2008).
[52] L. X. Liu *et al.*, Chin. Phys. Lett. **26**, 090402 (2009).
[53] P. R. Saulson, Phys. Rev. D **42**, 2437 (1990).
[54] SS316, Grade 200, Salem Specialty Ball Company, Inc., USA.
[55] PR-2004, Mettler Toledo company, Switzerland.
[56] J. Luo *et al.*, Chin. Phys. Lett. **18**, 1012 (2001).
[57] D. C. Chen *et al.*, Chin. Phys. Lett. **21**, 33 (2004).
[58] ELCOMAT vario 140/40, Möller-Wedel Optical Gmbh, Germany.
[59] JJG 146-2003, Verification Regulation of Gauge Block, National Institute of Metrology, China.
[60] DTP-1000B, Guangzhou Wilson Precision Instruments Co. Ltd., Guangzhou, China.
[61] JC08YQ8261, No. 6114 second class metrology institute of National Defense Science and Technology Industry.
[62] J. Q. Guo *et al.*, Chin. Phys. Lett. **21**, 612 (2004).
[63] FEI-Quanta 200, FEI Philips company, Holland.
[64] L. X. Liu *et al.*, Chin. Phys. Lett. **26**, 010403 (2009).
[65] MAG-03DAM, Bartington Instruments Ltd., Britain.
[66] ELCOMAT 3000, Möller-Wedel Optical Gmbh, Germany.
[67] PCI-6014, National Instruments company, USA.
[68] EE1620C, Nanjing Telecommunication Instruments Factory, Nanjing, China.
[69] SR620, Stanford Research Systems Company, USA.
[70] SR540, Stanford Research Systems Company, USA.
[71] One-dimensional position-sensitive photocell (model SD-1166-21-391), Silicon Detector Corporation, Newbury Park.
[72] SR830, Stanford Research Systems Company, USA.
[73] CST6502, Beijing ConST Instruments Technology Inc., Beijing, China.
[74] G. E. Uhlenbeck and L. S. Ornstein, Phys. Rev. **36**, 823 (1930).
[75] M. C. Wang and G. E. Uhlenbeck, Rev. Mod. Phys. **17**, 323 (1945).
[76] R. C. Ritter and G. T. Gillies, Phys. Rev. A **31**, 995 (1985).
[77] Y. T. Chen and A. Cook, Classical Quantum Gravity **7**, 1225 (1990).
[78] G. T. Gillies and R. C. Ritter, Rev. Sci. Instrum. **64**, 283 (1993).
[79] R. C. Ritter, L. I. Winkler, and G. T. Gillies, Meas. Sci. Technol. **10**, 499 (1999).
[80] J. Luo, C. G. Shao, and D. H. Wang, Classical Quantum Gravity **26**, 195005 (2009).
[81] C. Zener, *Elasticity and Anelasticity of Metals* (University of Chicago Press, Chicago, 1948).
[82] J. Luo, Z. K. Hu, and H. Hsu, Rev. Sci. Instrum. **71**, 1524 (2000).
[83] Z. K. Hu, X. L. Wang, and J. Luo, Chin. Phys. Lett. **18**, 7 (2001).
[84] F. Chen *et al.*, Meas. Sci. Technol. **14**, 619 (2003).
[85] C. G. Shao, E. J. Luan, and J. Luo, Rev. Sci. Instrum. **74**, 2849 (2003).
[86] Y. L. Tian, Y. Tu, and C. G. Shao, Rev. Sci. Instrum. **75**, 1971 (2004).
[87] A. H. Nayfeh and D. T. Mook, *Nonlinear Oscillations* (Wiley, New York, 1979).
[88] Y. T. Chen, Phys. Lett. **106A**, 19 (1984).
[89] Z. K. Hu, J. Luo, and H. Hsu, Phys. Lett. A **264**, 112 (1999).
[90] Z. K. Hu and J. Luo, Phys. Lett. A **268**, 255 (2000).
[91] S. Q. Yang *et al.*, Phys. Rev. D **80**, 122005 (2009).
[92] M. K. Bantel and R. D. Newman, J. Alloys Compd. **310**, 233 (2000).
[93] Q. Li *et al.*, Chin. Phys. Lett. **27**, 070401 (2010).
[94] U. Klein, W. Vollmann, and P. J. Abatti, IEEE Trans. Ed. **46**, 338 (2003).
[95] C. C. Speake, Classical Quantum Gravity **13**, A291 (1996).
[96] C. C. Speake and C. Trenkel, Phys. Rev. Lett. **90**, 160403 (2003).
[97] K. Numata *et al.*, Phys. Lett. A **327**, 263 (2004).
[98] K. Numata, J. Horowitz, and J. Camp, Phys. Lett. A **370**, 91 (2007).
[99] R. D. Rose *et al.*, Phys. Rev. Lett. **23**, 655 (1969).
[100] J. H. Gundlach, E. G. Adelberger, B. R. Heckel, and H. E. Swanson, Phys. Rev. D **54**, R1256 (1996).
[101] J. H. Gundlach, Meas. Sci. Technol. **10**, 454 (1999).
[102] E. R. Cohen and B. N. Taylor, J. Phys. Chem. Ref. Data **2**, 663 (1973).
[103] E. R. Cohen and B. N. Taylor, Rev. Mod. Phys. **59**, 1121 (1987).